2. Elements of Physical Oceanography

Wendell S. Brown

This chapter discusses the most important elements of physical oceanography in terms of the various oceanic responses to atmospheric and astronomical forcing – as mediated by earth rotation, including surface, and internal gravity waves; inertial motion and hurricane-driven storm surge. We include an outline of the history of wind-generated surface waves: generation to dissipation on the beaches. The roles of turbulence-derived oceanic friction in Ekman dynamics/upwelling-downwelling are outlined. There is a discussion of the elements of practical tidal sea level prediction. There is a review of the central role of geostrophic flow in wind- and thermohaline-driven circulations on ocean basin as well as continental shelf scales.

The ocean environment consists not only of the water column, but also the atmosphere above the water's surface and the seafloor and sediment and rocks of the subseafloor. A comprehensive study of the marine environment is enormous in scope and is thus often subdivided into disciplinary components, including biology, chemical, geology, physics, and meteorology. This chapter will focus on basic introductory information concerning aspects of the marine environment; however, it will also refer oceanographic literature for those seeking more comprehensive treatments.

Different aspects of ocean engineering design are influenced to varying degrees by one or more environmental factors. These factors comprise one of the several groups of the so-called external *design* constraints; or constraints that are independent of or external to the purpose on which the design is based. For example, submersibles encounter temperature, salinity, pressure, and density gradients as they move through the water column, irrespective of their individual missions. These *external constraints* may be subdivided into those which are fixed by mission requirements and those which are variable. For example, the design *maximum operating depth* of a submersible sets the maximum pressure that the submersible can encounter. However, this operating constraint is not usually linked to specific values of sea water temperature, salinity, and density which can be encountered; but rather only ranges of these variables.

While discussing different oceanic environmental factors, it is convenient to consider them in terms of the three basic regimes in a vertical profile that includes the atmosphere and the water column.

2.1 Atmospheric Processes

An instantaneous snapshot of the winds of the entire atmosphere would present an extremely chaotic view of the flow. Atmospheric circulations can be characterized as an enormously complex patterns of *eddies within eddies*. Thus, it is convenient to categorize the different features of atmospheric circulations according to their different sizes – or scales of motion.

The very small-scale eddies or whirls with time scales of only a few seconds can be eliminated by averaging the measured winds over periods of several minutes. Furthermore, observations are so widely spaced in time and area that most must be considered averages over horizontal distances of tens of kilometers, and vertical distances of tens of meters. Thus, even such relatively large circulation phenomena as thunderstorms and tornadoes often cannot be resolved by the usual weather station network of observations. Through this kind of averaging the range of atmospheric motions can be classified in terms of three general scales; microscale, mesoscale, and synoptic scales (Fig. 2.1).

On the microscale, we find small, short-lived eddies (or turbulence), that are strongly affected by local conditions of both surface roughness and temperature. These eddies are very significant as dispersers of pollutants. At the large end of the microscale are tornadoes and waterspouts. Because microscale motions have such short time scales, Earth rotation is not a significant factor.

Mesoscale phenomena of intermediate horizontal size include such processes as land–sea breezes, thunderstorms, and squall lines. Earth rotation can be an important factor affecting the larger mesoscale phenomena such as sea breezes.

Synoptic scale phenomena most notably represented by large-scale, low-pressure cyclones and high-pressure anticyclones that control our day-to-day weather changes – particularly at mid-latitudes. Historically these synoptic-scale features have been defined every 3 h by the large-scale weather network of simultaneous observations. Earth rotation-related forces are very important factors in the physics of synoptic-scale systems, which persist for days to weeks. Synoptic-scale features that persist for weeks to months tend to have planetary space scales and like jet stream loops play an important role in determining the seasonal characteristics of the weather.

The vertical displacements distinguish these different scales of atmospheric motion. For example, synoptic scale phenomena are dominated by horizontal motions; with vertical velocities generally only 1 to 2 cm/s. Even the great cyclonic storms in the middle and high latitudes, have vertical velocities of the order of 50 cm/s. In the smaller, more intense mesoscale circulations, horizontal and vertical velocities are more comparable; with thunderstorm vertical velocities are often of the order of 10 m/s. Microscale or turbulent phenomena, with nearly equal horizontal and vertical velocities, occur principally in a rather shallow layer adjacent to the Earth's surface and thus are important factors in air–sea interactions. A detailed description of the maritime atmosphere is provided in Chap. 3.

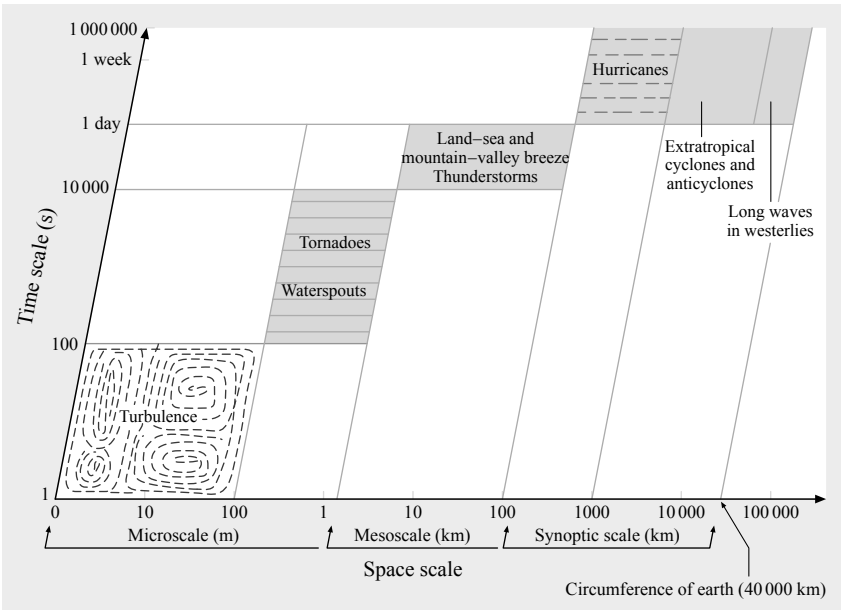

Fig. 2.1 Horizontal space and time scales of atmospheric circulations (after [2.1])

2.2 Ocean Structure

The global atmosphere and the ocean interact in ways that structure the ocean into fairly distinct *upper ocean layer*, which extends down to about 1000 m (3284 ft), and *deep ocean layer*, which extends to the bottom. On one hand, air–sea interactions create vast amounts of sinking cold, dense water in the polar oceans north and south of 40° latitude. On the other hand, in the subtropical and tropical regions between 40°S and 40°N, air–sea interactions warms a buoyant upper layer of the ocean that overlies a deep layer of cold, dense water throughout the world's oceans. The contoured-density section the Atlantic Ocean in Fig. 2.2 highlights the 2 layers. In particular, the region of closely packed of the isopycnals – the pycnocline – in the upper few 100 m represents a dynamical barrier to vertical mixing between upper and deep layer of the ocean.

The trio of oceanic water column density profiles in Fig. 2.3 demonstrates how the strength of the pynocline in the equatorial/tropical water column is much stronger than that in the high latitude polar regions. Density or specific weight of sea water is a function of temperature, salinity, and pressure. Variations in sea water temperature and salinity (which determine density) vary substantially in the upper layer water column forming their respective thermoclines and haloclines. These variations, in general, are due to the influences of heat exchange and precipitation/evaporation across the air–sea interface at a particular latitude and season. In the deep ocean layer, below 1000 m, these characteristics tend to be relatively constant. The upper ocean layer may be subdivided further into regions of seasonal and main pycnocline (and corresponding thermoclines and haloclines); particularly in the subtropics between 20° and 40° latitudes where density/temperature/salinity gradients are largest extending, respectively, from the surface to about 60 m and from this depth to about 1000 m (Fig. 2.4).

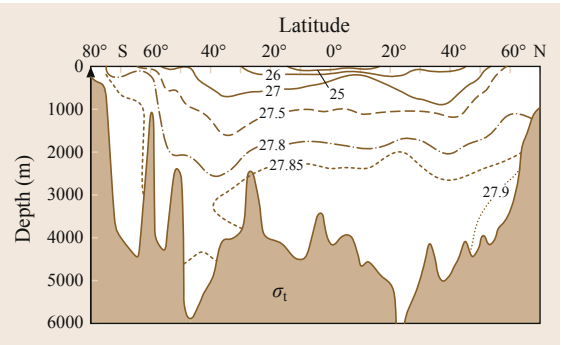

Fig. 2.2 A south–north section of contours of density anomaly (σ_t = water density − 1000) in the western Atlantic; showing how the upper and lower layers of the ocean between 50°S and 50°N are defined by closely packed isopycnals – a strong pycnocline or density stratification – at a depth of about 800 m (after [2.2])

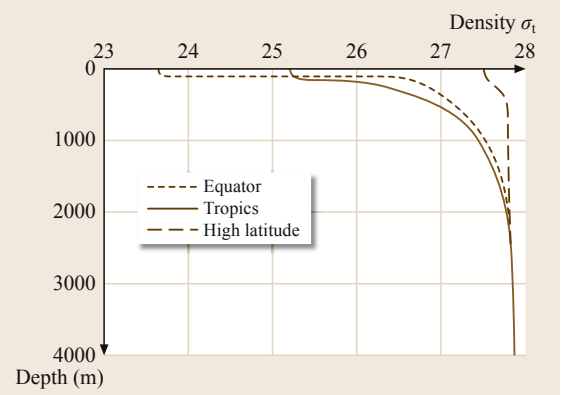

Fig. 2.3 Typical density anomaly versus depth profiles at low and high latitudes (after [2.2])

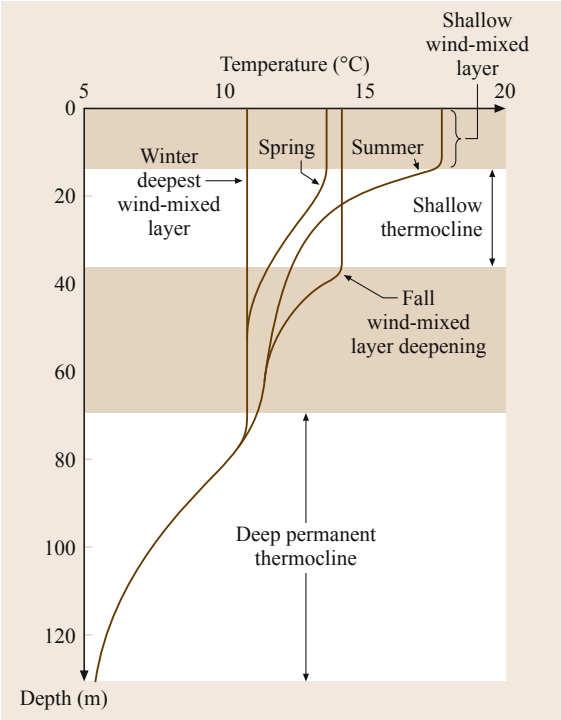

Fig. 2.4 The seasonal variability of a typical subtropical temperature profile (after [2.3])

2.3 Oceanic Processes

Like the atmospheric winds, ocean currents at a single place/time is a superposition of contributions from a complex set of processes many with different space-time scales. The following profiles many of the most important ocean processes in terms of their basic physical elements including forcing and restoring forces and relevance in the overall ocean system. The corresponding ranges of time and space scales of these processes are presented in Table 2.1 and in the dispersion diagram (Fig. 2.5) – a diagram that is particularly relevant to waves:

- Capillary waves. *Physics: surface tension, inertia, wind-driving* – First effect of winds in wave generation
- Surface gravity waves (short). *Physics: gravity, inertia, wind-driving* – Mid-ocean wind waves/surface chop, shipping, off-shore construction.
- Surface gravity waves (long). *Physics: gravity, inertia, bottom topography, wind-driving or earthquake* – Surf and breakers, storm surges, tsunamis, dangerous flooding.
- Internal gravity waves. *Physics: gravity or buoyancy, inertia, topography, indirect wind- driving* – Energy dissipation, mooring stresses, *dead water*.
- Turbulence, mixing. *Physics: inertia, buoyancy, nonlinear interaction, friction* – Dissipation of energy, mixing of momentum and dissolved chemicals including O_2.
- Upwelling (and downwelling). *Physics: buoyancy, local winds and currents* – Brings up nutrients/formation of water masses.
- Mid-Ocean mean flows. *Physics: buoyancy, Coriolis force, wind and heating driving, friction* – Maintaining climate, distributing chemicals, and heat for biology.
- Continental shelf currents. *Physics: buoyancy, Coriolis force, nonlinear inertia* – Transfer of heat and vorticity, climate and local weather, biology, chemistry.
- Tides. *Physics: gravity, inertia, sun and moon gravitational pull, Coriolis force* – Piloting and shipping, coastal construction.
- Internal tides. *Physics: gravity or buoyancy, inertia, topography, indirect wind-driving* – Internal waves at tidal periods with large vertical excursions.
- Estuary flows. *Physics: gravity-buoyancy, Coriolis, tidal, and wind forcing* – Pollutant dispersal, biological nutrient renewal, inflow of fresh water.

The energy distribution of these different oceanic processes tends to sort by time scale and can be conveniently presented in terms of frequency spectra in different forms. The energy density (i. e., energy per unit

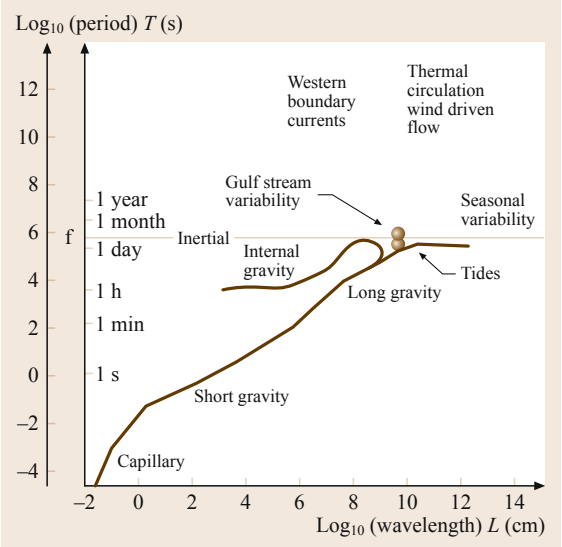

Fig. 2.5 Dispersion diagram for the principal oceanic processes

Table 2.1 Characteristic time and length scales associated with different ocean processes and currents

Type	Time Scales T	Length Scales L	Amplitude H
Capillary waves	< 0.1 s	< 1 cm	< 1 cm
Short surface gravity waves	0.1–60 s	cm–km	m
Long surface gravity waves	s/h	m–10's km	m
Internal gravity waves	min–h	m–10's km	m
Turbulence (Mixing)	s	cm–m	mm–cm/s
Upwelling/downwelling	Days–seasonal	100 km < 1	mm/day
Mid-ocean *mean* flow	1000km	1000 km	cm/s
Western boundary currents	Seasonal–decadal	100 km	≈ 200 cm/s
Continental shelf currents	Days–months	100 km	cm/s
Tides	Day	1000 km	m
Internal tides	Day	10–100 km	10 m
Estuarine currents	Day–seasonal	100 km	cm/sec

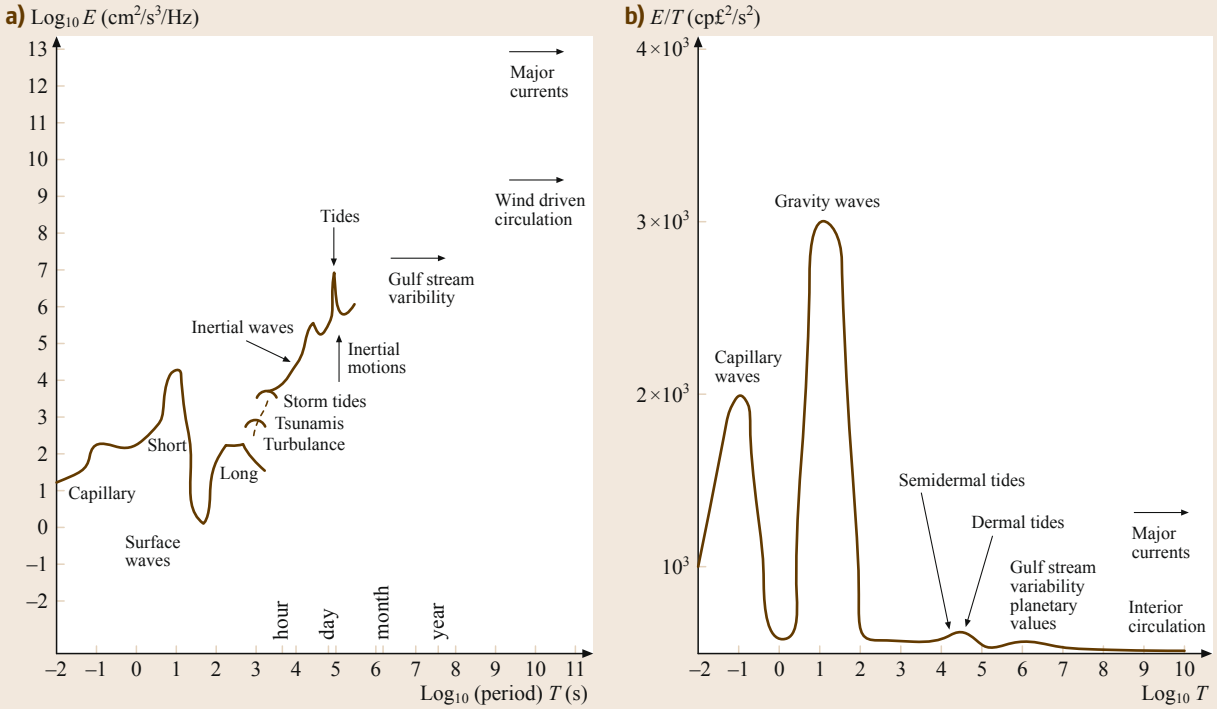

Fig. 2.6a,b **(a)** An *energy density spectrum* (EDS) of ocean current variability highlights the distinctive periodicities associated with many important oceanic processes. **(b)** The variance-preserving form of the corresponding EDS displays the period distribution of kinetic energy per unit ocean volume of these oceanic processes

frequency bandwidth) spectrum highlighting a range of principal ocean processes is presented in Fig. 2.6a. However, the corresponding *variance-preserving form* of the energy spectrum (Fig. 2.6b) is more useful for comparing the kinetic energy per unit volume of these different processes. Clearly energy concentration in physical space is greatest for surface gravity waves with capillary waves a close second. The next section treats the important class of surface gravity waves in more depth.

2.4 Surface Gravity Waves

Very often winds disturb the sea surface; leading to the generation a surface gravity waves with a broad range of wave periods. The gravitational interactions of the moon (and sun) with the Earth also disturb the sea surface in generating surface tidal waves. Tidal current interactions with bathymetry generate internal tides, which, if very nonlinear may spawn packets of internal solitons.

In all of these cases, as gravity acts to restore the sea surface distortion toward its equilibrium state, the potential energy of the original distortion is converted to kinetic energy in the form of a velocity field. The lowering sea surface then overshoots the equilibrium state as the gravity-related buoyancy forces reverse the process. As these surface gravity waves are generated, they with their energy propagate away from their generation site.

The wave periodogram in Fig. 2.7 shows how surface wave energy is distributed among many wave frequencies in the ocean. Wind-driven surface gravity waves of wind periods in the 1−30 s range are the most energetic, followed by tides. Note that short period (or high frequency) capillary wave motion is controlled by surface tension, while longer period (or low frequency) gravity waves, like storm surges and tides, are also influenced by earth rotation.

2.4.1 Surface Gravity Waves

The currents and pressures associated with surface gravity waves are attenuated with depth in accordance with their wavelength. The current and pressure amplitudes of surface waves become negligible (less than 5% of their surface values) at a depth of $L/2$, where L is the

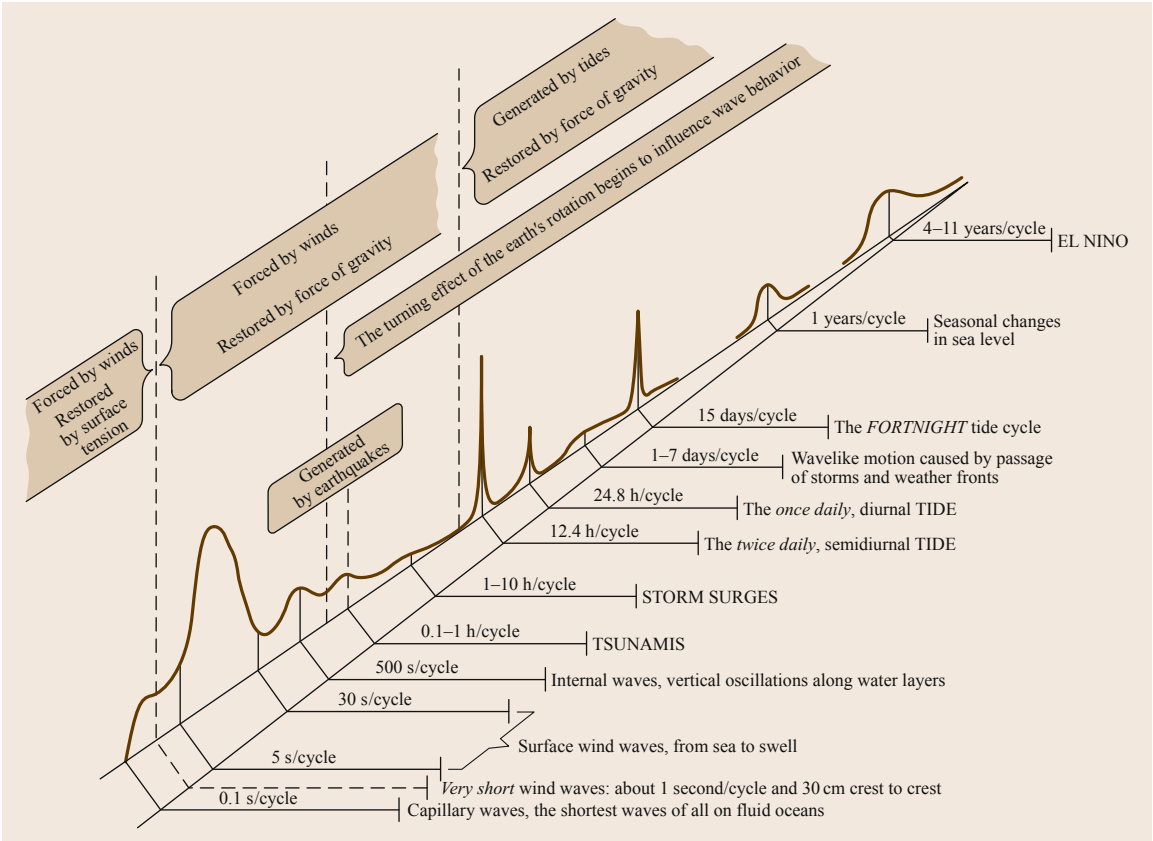

Fig. 2.7 This periodogram of sea level variability diagrams how energy of many different types of ocean gravity waves is distributed according to frequency. Waves are identified according to wave period and to the disturbing and restoring forces which act at different time scales (after [2.4])

wavelength. The currents associated with typical deep water wind waves (period of 20 s) are effectively attenuated at depths of about 300 m (984 ft) and are almost never felt at depths of 1000 m (3284 ft).

However, the longer period tides and tsunamis have such large wavelengths that their effects are virtually unattenuated throughout most of the world's oceans. However, because their periods are so much longer (minutes to a day) than typical wind waves, the water velocities associated with them are generally small. Tidal currents in coastal oceans settings are an important exception.

2.4.2 Definitions

Here we consider a simplified model for surface gravity waves. As we all have observed the sea surface at a particular location is a complicated superposition of waves with different characteristics propagating from different places where they were usually generated by the wind at different times. However, first we want to focus on the basic principles of wave motion, so we will explore a simple monochromatic (i. e., single frequency) wave model. Later, we will apply this understanding of the *essential physics* of wave motion to more realistic observed wave fields.

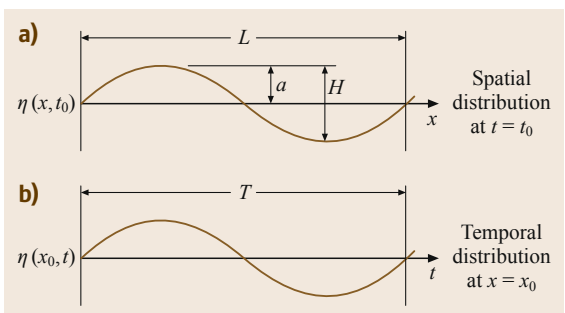

Fig. 2.8a,b The characteristics of a monochromatic sine wave $\eta(x, t)$ whose form is propagating with phase speed c in the x-direction is **(a)** *frozen* in space at time $t = t_0$; and **(b)** measured at a fixed station $x = x_0$

To start, we define the characteristics (with units indicated in [. . .]) of the monochromatic sine wave shown in Fig. 2.8:

- Elevation: $\eta(x, t)$ is the instantaneous vertical departure of the sea level from the undisturbed sea level.
- Wave height: H is the distance between the wave crest and trough. $[H] = (\text{unit length})^{-1}$
- Wave amplitude: $a = 1/2H$
- Wavelength: L is the distance between points of equal phase. $[L] = \text{length}$
- Wave number: $k = 2\pi/L$ is the number of times a wave can fit on the circumference of circle with a dimensionless radius = 1. $[k] = (\text{length})^{-1}$
- Wave period: T is the time between points of equal phase. $[T] = \text{unit time}$.
- Wave frequency: $f = 1/T$ is the number of complete cycles per unit time. $[f] = \text{cycles/time}$
- Angular frequency: $\omega = 2\pi/T = 2\pi f$ is the number of times a wave of period T can fit on the circumference of a circle with a dimensionless radius = 1. $[\omega] = (\text{time})^{-1}$
- Wave phase speed: $c \equiv L/T$ or $c \equiv \omega/k$ is the speed of a particular point on the waveform (or phase). $[c] = \text{length/time}$

The mathematical description of our monochromatic *right-traveling* waveform is

$$\eta(x,t) = a\cos\left(\frac{2\pi x}{L} - \frac{2\pi t}{T}\right)$$

or

$$= a\cos(kx - \omega t)\,. \tag{2.1}$$

Equation (2.1) can also be written in terms of phase speed as $\eta(x,t) = a\cos[k(x - ct)]$. The dynamical relation between wave period T and wavelength L can be defined by the solution to the two-dimensional (2-D) *Airy wave model* of a right-traveling wave at the surface of an ocean (mean depth $z = 0$) with a flat bottom at a depth of $-z = h$.

The solution to the approximate linearized Airy wave equations of motion and boundary conditions for small amplitude ($a/L \ll 1$) waves [2.5] yields the *dispersion relation*

$$\omega^2 = gk\tanh(kh)\,, \tag{2.2}$$

which describes the relation between wave frequency and wave number, and the dynamical variables of pressure p, and the x- and upward ($+z$)-directed velocity components u and w, respectively:

$$u = a\omega\frac{\cosh k(z+h)}{\sinh(kh)}\cos(kx - \omega t)\,, \tag{2.3a}$$

$$w = a\omega\frac{\sinh k(z+h)}{\sinh(kh)}\sin(kx - \omega t)\,, \tag{2.3b}$$

$$p = -\rho gz + \rho ga\frac{\cosh k(z+h)}{\cosh kh}\cos(kw - \omega t)\,. \tag{2.3c}$$

The dispersion relation given above can be rewritten as

$$c^2 = \frac{L^2}{T^2} = \frac{\omega^2}{k^2} = \frac{g}{k}\tanh(kh)\,,$$

which shows that, in general, Airy waves have phase speeds which depend upon wave number k (or wavelength L) (Fig. 2.9).

Two important approximations to the (2.2) and (2.3) wave solutions yield the classical *short* and *long* waves which are defined in terms of the wavelength to water depth ratio L/h.

For *short waves*, the water depth is greater than a half wavelength $h > L/2$ so that they are referred to as *deep water waves*. Mathematically, this means that kh is large (or $kh > \pi$) so that the *short wave* (deep water wave) dispersion relation (2.2) becomes

$$c^2 = \frac{\omega^2}{k^2} = \frac{g}{k} = g\frac{L}{2\pi}\,,$$

which reduces to

$$c = \sqrt{\frac{1}{2\pi}(gL)}\,,$$

so that short waves are dispersive, that is, the wave speed depends on wavelength. Since $L = cT$, the above

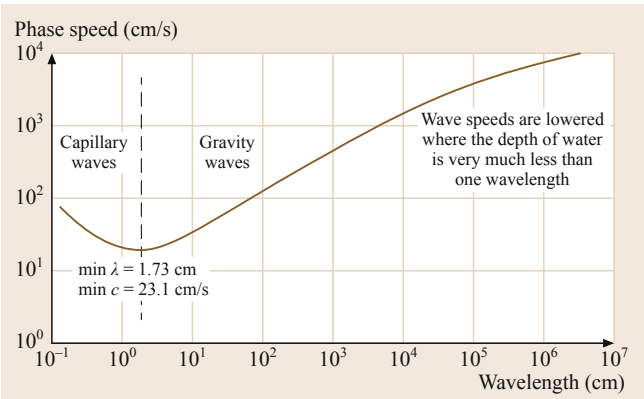

Fig. 2.9 The phase speed of gravity waves and capillary waves as a function of their wavelength (after [2.6])

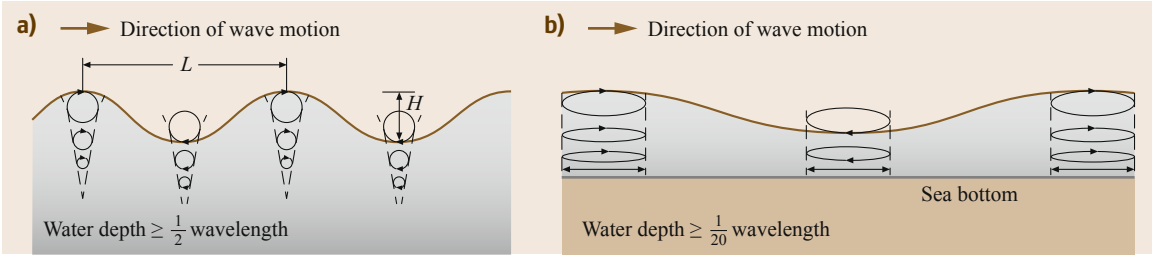

Fig. 2.10a,b **(a)** Progressive deep-water wave motion consists of near-circular water parcel orbits that become very small at water depths of $1/2$ wavelength. **(b)** Progressive shallow water wave motion ($h/L > 0.05$) is distinguished by water parcels that move in highly elliptical orbits, with widths that are constant with depth (after [2.7])

can also be written as

$$c = \frac{1}{2\pi}(\mathrm{g}T) \, .$$

For large kh, the *short wave solutions* to (2.3) for $\eta = a\cos(kx - \omega t)$ become

$$u = a\omega \mathrm{e}^{kz}\cos(kx - \omega t) \, ,$$

$$w = a\omega \mathrm{e}^{kz}\sin(kx - \omega t) \, ,$$

$$p = \rho g a \mathrm{e}^{kz}\cos(kx - \omega t) - \rho \mathrm{g} z \, .$$

The motions associated with short or deep water waves decreases with depth, such that amplitudes at a depth of $z = -L/2$ are $\mathrm{e}^{-\pi}$, or 4% of surface values. This is shown in the schematic of the water parcel trajectories as the wave passes (to the right in this case, Fig. 2.10a).

For *long waves*, the water depth is less than the wavelength or $h < L/20$ so that long waves *feel the bottom* and are called *shallow water waves* (Fig. 2.10b). Mathematically, this means that kh is small (or $kh > \pi/10$) so that the *long* (shallow water) *wave* dispersion relation (2.2) becomes

$$\tanh(kh) \approx kh \, ,$$

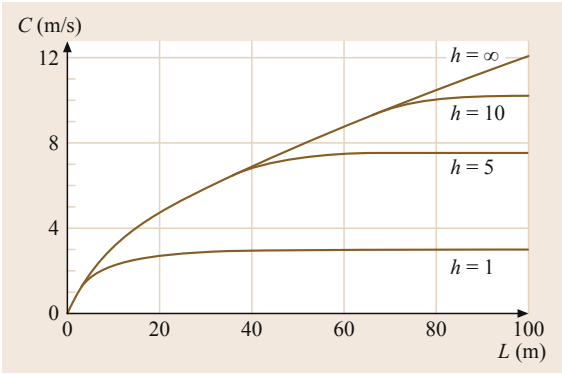

Fig. 2.11 Wave phase speed c versus wavelength L (m) – a dispersion diagram for Airy waves in different water depths h (m)

and the *long wave* (shallow water) dispersion relation becomes

$$c^2 = \frac{\omega^2}{k^2} = \frac{\mathrm{g}}{k}kh$$

or

$$c = \sqrt{\mathrm{g}h} \, .$$

Thus, long (or shallow water) waves are *nondispersive*, that is that their speed is independent of wavelength. This is demonstrated in Fig. 2.11 which depicts the relation of wave phase speed and wavelength for different water depths.

For small kh, the *long wave* (shallow water) pressure and horizontal velocity *solutions* to (2.3) for $\eta = a\cos(kx - \omega t)$ are undiminished with depth. The water parcel orbits during the passage of a *long water wave* in very shallow water are very elliptical as shown in Fig. 2.10b. Notice that most of the motion is horizontal, much like what scuba divers feel in shallow water with a long swell. Airy wave kinematics are shown schematically in Fig. 2.12 for different water depths. Note the relative phases of η, u, and w fields.

As Airy waves propagate from deep water through intermediate depth water into shallow water (Fig. 2.13), (2.2) and (2.3) describe their dynamics. As deep water waves propagate into shallow water, their orbital motions and pressure fields begin to interact with the bottom – they *feel the bottom*. Nearly circular water parcel orbits become more elliptical and wave velocities induce bottom stresses; which can have an effect on movable sediments.

However, while monochromatic Airy wave theory is very helpful in describing the basic dynamic characteristics of waves, the real ocean wave field is composed of contributions from waves with many wavelengths, wave periods and amplitudes. What are the consequences of the superposition of more than one Airy wave?

To answer the question, we increase the complexity of our model slightly by superposing two Airy waves η_1 and η_2 with the same amplitude but slightly different

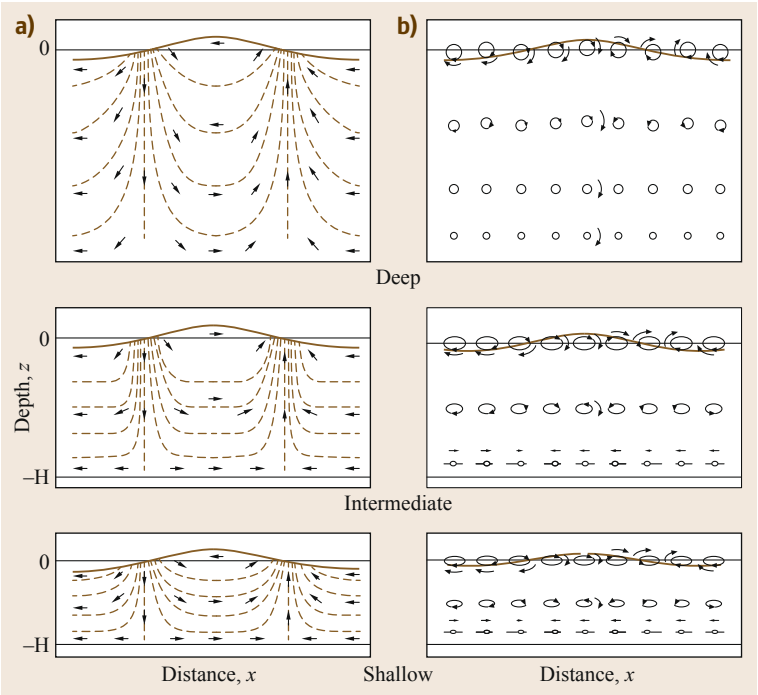

Fig. 2.12a,b Kinematics of waves propagating left to right in (top) deep; (middle) intermediate depth; and (bottom) shallow water – **(a)** instantaneous snapshots of the water parcel streamlines and **(b)** trajectories of selected water parcels over a full wave cycle (after [2.8])

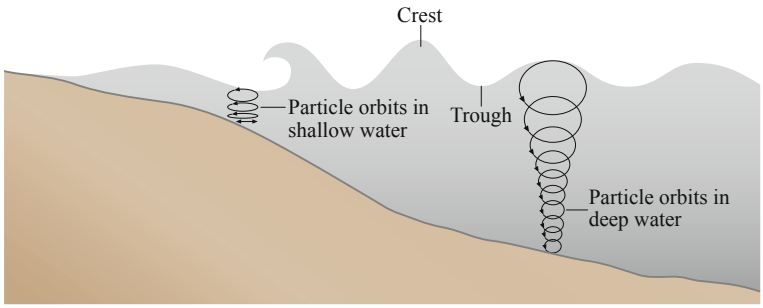

Fig. 2.13 Deep water waves propagating toward the left into *shallow water*. Note how the waves *feel the bottom* and water parcel orbits are squashed as the wave propagates into even shallower water

frequencies and wave numbers such that $\omega_2 > \omega_1$ and $k_2 > k_1$.

The amplitude of the resultant wave (shown in Fig. 2.14) is modulated according to

$$\eta = a\cos\left[\frac{\Delta k}{2}(x - c_g t)\right]\cos\left[\overline{k}(x - \overline{c}t)\right] , \qquad (2.4a)$$

where

$$\overline{k} = \frac{k_1 + k_2}{2}, \quad \overline{c} = \frac{\overline{w}}{\overline{k}} \quad \text{and} \quad \overline{\omega} = \frac{\omega_1 + \omega_2}{2} . \qquad (2.4b)$$

Note that on one hand, the cos[ ] term on the right in (2.4) represents a wave with intermediate frequency and wavelength and therefore is nearly indistinguishable from the parent waves. On the other hand, the cos[ ]

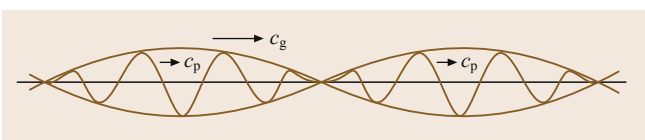

Fig. 2.14 The wave envelope – resulting from the superposition of a pair of surface gravity waves (with nearly identical phase speeds c_p) – travels at the wave group velocity c_g

term on the left represents a wave with much greater L (smaller k) that is traveling at the speed c_g given by

$$\frac{\Delta\omega}{\Delta k} = \frac{\omega_2 - \omega_1}{k_2 - k_1} = c_g .$$

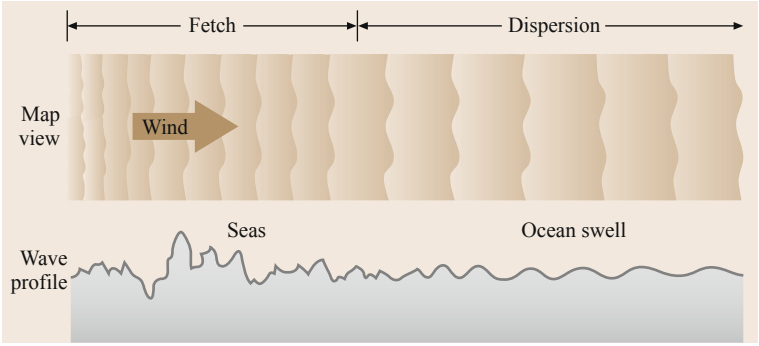

Fig. 2.15 As the wind increases from zero over a *glassy* ocean surface, first capillary waves are generated; which very rapidly evolve into ripples, chop, wind waves, and eventually a fully developed sea (after [2.7])

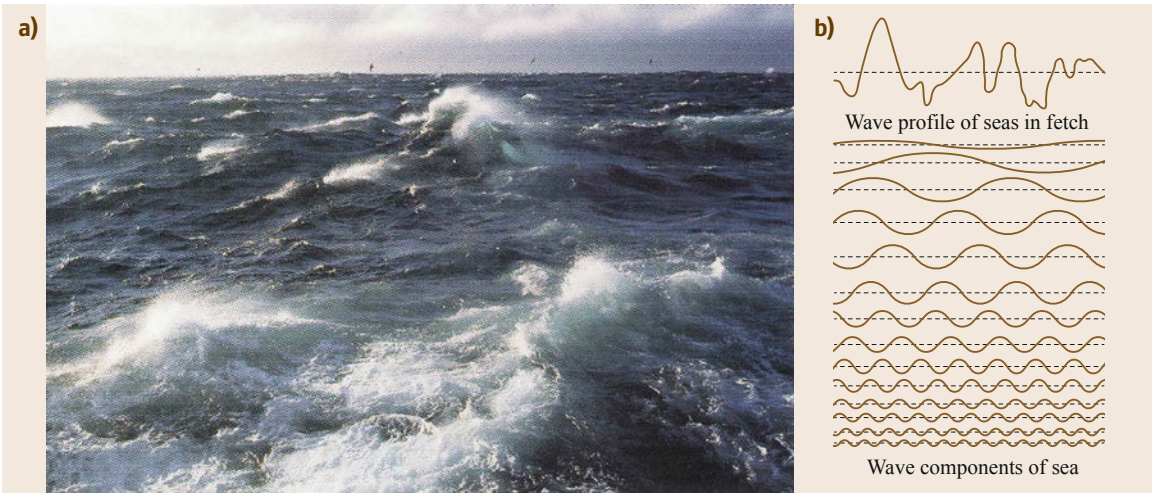

Fig. 2.16 **(a)** The open ocean sea surface is generally chaotic because it is **(b)** a superposition of many different waves, with different wavelengths and heights (after [2.7])

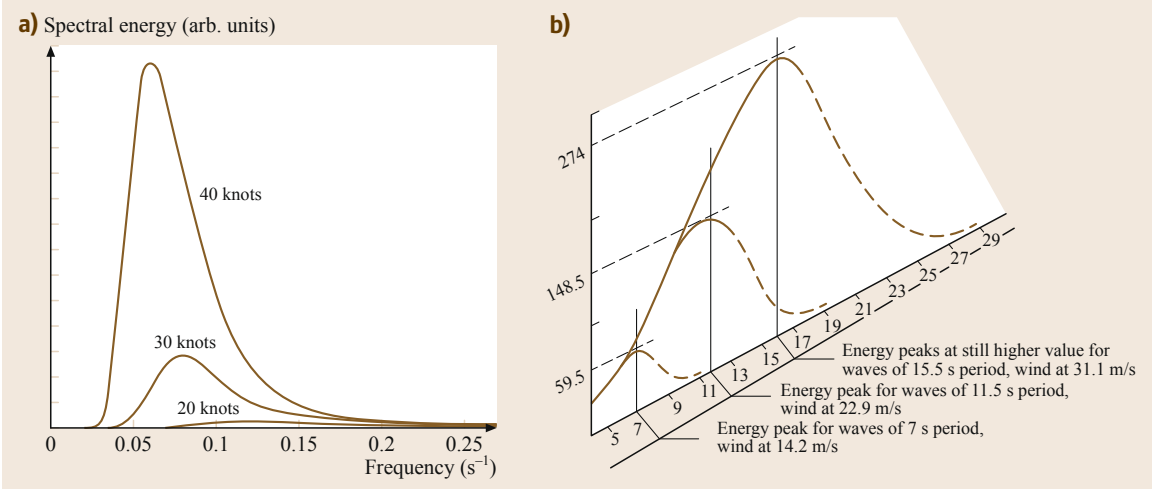

Fig. 2.17 **(a)** A frequency spectra of the wave *energy density*(variance per unit frequency bandwidth) for a fully developed sea under different wind speed conditions. Note how the larger wind speeds generate waves for which the energy density peak is at lower frequencies (after [2.8]). **(b)** A *periodogram* of *wave energy* (kJ/m^2) for fully developed wave fields generated by different wind speeds – derived from Table 2.2 data (after [2.4])

Table 2.2 Examples of the characteristics of wind waves observed for fully developed seas under different wind conditions (after [2.9])

Wind speed [m/s]	Wave phase speed [m/s]	Wave period [s]	Wavelength L [m]	Wave height H [m]	H/L	Energy [kJ/m^2]
14.2	11.5	7.0	78.0	6.9	0.088	59.5
16.0	12.8	8.0	103.0	7.7	0.074	74.1
19.2	16.3	9.5	147.0	9.2	0.063	106.0
22.9	18.3	11.5	209.0	10.9	0.052	148.5
27.0	21.5	13.5	290.0	13.0	0.045	211.0
31.1	25.0	15.5	384.0	14.8	0.039	274.0

Table 2.3 Conditions necessary for fully developed sea at given wind speed and the parameters of the resulting waves (after [2.9])

Wind speed [knots]	Fetch [nautical miles]	Duration [h]	Average height [ft]	[m]	Average length [ft]	[m]	Average period [s]
10	10	2	0.9	0.27	28	8.5	3.0
12	18	4	1.4	0.43	40	12.2	3.4
14	28	5	2.0	0.61	55	16.8	4.0
16	40	7	2.8	0.85	71	21.6	4.6
18	55	8	3.8	1.2	90	27.4	5.0
20	75	10	4.9	1.5	111	33.8	5.7
22	100	12	6.3	1.9	135	41.2	6.3
24	130	14	7.8	2.4	160	48.8	7.0
26	180	17	9.5	2.9	188	57.3	7.4
28	230	20	11.4	3.5	218	66.4	8.0
30	280	23	13.6	4.1	251	76.5	8.6
32	340	27	16.0	4.9	285	86.9	9.0
34	420	30	18.6	5.7	322	98.2	9.7
36	500	34	21.4	6.5	361	110.1	10.3
38	600	38	34.5	7.5	402	122.6	10.9
40	710	42	27.9	8.5	446	136.0	11.4
42	830	47	31.5	9.6	491	149.7	12.0
44	960	52	35.4	10.8	540	164.6	12.6

In general, the superposition of multiple surface gravity waves form packets called *wave groups* whose energy travels at the *group speed* given by $c_g = \mathrm{d}\omega/\mathrm{d}k$. Thus the group velocity for general Airy waves is

$$c_g = \frac{1}{2}c\left(1 + \frac{2kh}{\sin h2kh}\right) ,$$

which for short waves (large kh) becomes

$$c_g = \frac{1}{2}c\,; \quad \text{deep water waves}$$

and for long waves (small kh) becomes

$$c_g = c; \quad \text{shallow water waves.}$$

Wave energy is composed of both the kinetic and potential energy components which can be computed explicitly for Airy waves [2.5]. In particular for shallow water waves, which are nondispersive, the wave energy travels at the same speed for all waves at $c = \sqrt{gh}$. The topic of wave generation and wave energy propagation is considered next.

2.4.3 Wave Generation and Evolution

Most ocean surface waves are produced by the wind. As the wind increases from near zero, it generates capillary waves, with short wavelengths (< 1.7 cm) and short periods (< 0.1 s). As the wind continues to blow, the

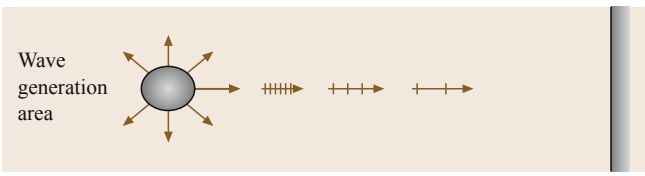

Fig. 2.18 Wave dispersion separates waves generated in the wave generation region

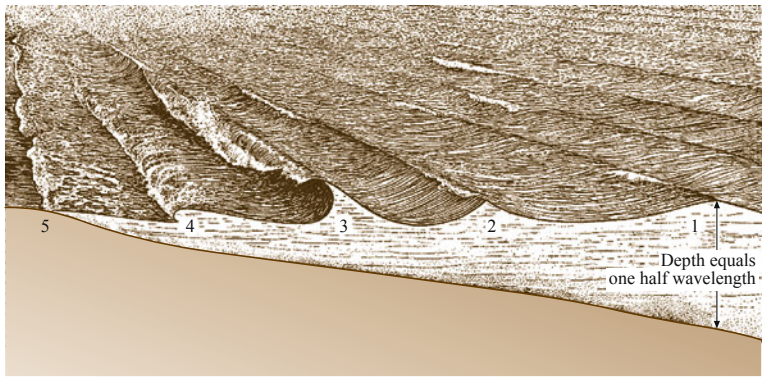

Fig. 2.19 (1) Deep water waves beginning to *feel the bottom*; (2) intermediate to shallow water wave transition; (3) shallow water waves begins to break; (4) fuel wave breaking; and (5) runup (after [2.10])

capillary waves can grow to become ripples and short choppy waves (Fig. 2.15). With increased wind velocity, duration, and fetch (length of the area over which the wind blows), more energetic (higher), longer waves are generated. The superposition of all of these waves in the wave generation region creates a fully developed sea with white capping. A fully developed sea appears chaotic because it is a superposition of waves with different wavelengths and corresponding wave periods (Fig. 2.16).

The spectral energy content of sea surface variability at the site can be analyzed in terms of their frequency content and displayed as energy density spectra (Fig. 2.17a) or a wave energy periodogram (Fig. 2.17b). These examples illustrate typical energy distribution as a function of wave frequency (or wave period) for a *fully developed sea* under different wind speeds. Both examples show generally that higher winds generate more energetic lower frequency waves. The wind strength, duration, and fetch determine the resulting range of wavelengths and wave amplitudes in the waves constituting the corresponding *fully developed* sea (Table 2.3).

Since weather systems move much faster than ocean wind waves, the storm winds will diminish over the immediate area of wave generation. Then this chaotic superposition of waves of different wave periods and wavelengths will propagate from the region in all directions at different speeds. Along a particular propagation trajectory, like that depicted in Fig. 2.18, groups of these deep ocean waves with the longer wavelengths (and thus the larger group velocities) will outrun the shorter wave groups. Because of deep water wave dispersion, wave energy spectra measured some distance from their generation site (e.g., a distant shore) will differ from those that are measured at a later time; as the slower, shorter wave groups arrive.

Eventually all of the deep water waves will propagate into water depths where they begin to *feel the bottom* (Fig. 2.19) and undergo significant changes. Once frictional contact begins, the wave changes in several ways simultaneously, namely the wave speed drops, its height increases, and its direction shoreward becomes more and more perpendicular to the beach line [2.4].

As these shallow water waves propagate shoreward both their phase and group speeds

$$c = c_g = \frac{L}{T} = \sqrt{gh}\,, \tag{2.5}$$

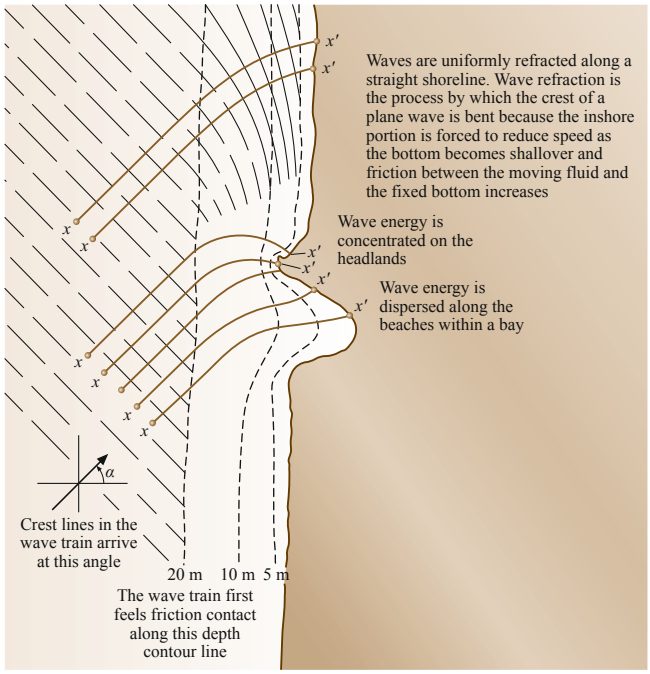

Fig. 2.20 Wave refraction or wavefront bending is due to the slowing of the part of the wavefront that shoals earliest. The pair of rays (or orthogonals that are perpendicular to the wavefront locally) mark the trajectory of equal amounts of wave energy (after [2.4]) ◄

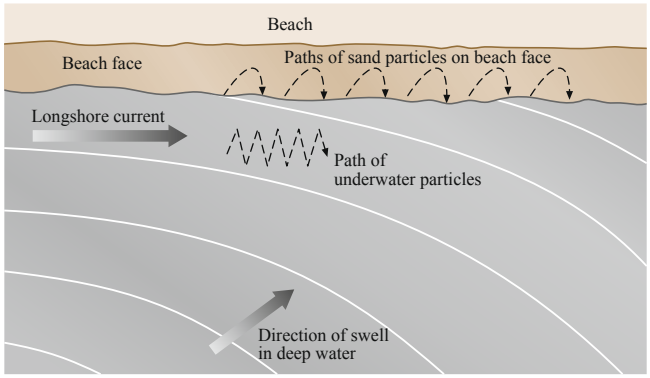

Fig. 2.21 Waves that approach the beach obliquely approach generates a longshore current in the surf zone. The wave-breaking suspends beach material (usually sand) that is transported in the surf zone by the longshore current; while the repeated wave run-up cycles also transport sand in the same longshore direction (after [2.10]) ►

decrease. Since the number of waves in the shoreward propagating wave train are conserved, the wave period T *remains constant*. Thus from a rearranged (2.5)

$$T = \frac{L}{\sqrt{gh}}\,, \tag{2.6}$$

the wavelength L must also decrease. For an idealized beach with straight coastline and parallel isobaths, the *wave power* per unit length of the shoreward propagating wavefront – given by

$$\overline{P} = \frac{1}{8}\rho g H^2 c_g = \frac{1}{8}\rho g H^2 \sqrt{gh} \tag{2.7}$$

is constant. Thus from a rearranged (2.7)

$$H^2 = \left(\frac{8\overline{P}}{\rho g^{3/2}}\right) h^{-1/2}\,, \tag{2.8}$$

we conclude that for shoreward propagating waves H must also increase! As a result, the wave slope which is proportional to H/L will increase to the point where Airy wave theory no longer applies.

At this stage, wave crests or fronts are generally propagating obliquely to the orientation of the beach (Fig. 2.20). The wavefronts are bent or refracted as the inshore end of the wavefront encounters even shallower water first and slows relative to the rest of the wave – bringing the wavefront into better alignment with the beach.

In the example of waves impinging on a straight beach (Fig. 2.20 – upper), by the refraction distorts the waves (and corresponding wave rays or orthogonals) so that the wave energy flux (energy/length/unit time) is reduced from its deep water value. Wave refraction near irregular coastlines (Fig. 2.20 – center) leads to distortion of the wavefronts. Thus the ray paths, or orthogonals indicating the direction of wave energy propagation, are also distorted. In the case of a *point of land* the equidistant rays in deep water are seen to converge on the point thereby concentrating wave energy there relative to other parts of the coastline. The opposite is true for a bay.

As the wave propagates shoreward, wave slopes generally increase and eventually lead to significant

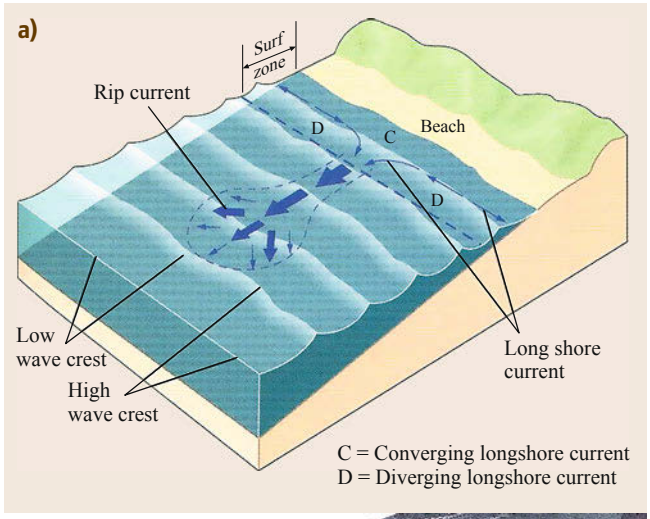

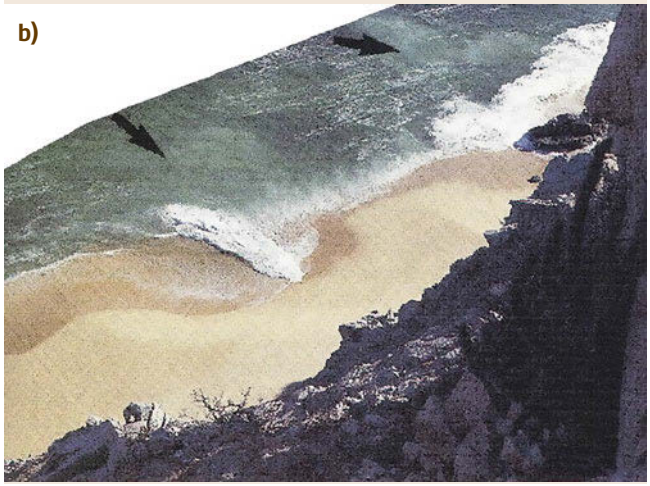

Fig. 2.22 **(a)** In this illustration, waves with crests parallel to the coast break and produce run-up that returns to the ocean via a system of longshore currents that feed narrow offshore rip currents. **(b)** narrow rapid rip current systems are observed frequently especially with large amplitude waves (after [2.7])

nonlinearities and subsequent *wave-breaking* as indicated at position 4 and *wave run-up* onto the beach front in position 5 in Fig. 2.19. It is noted that wave trains that approach the beach obliquely never fully align with the beach front. This asymmetry leads to the generation of an alongshore current in the direction indicated in Fig. 2.21. This alongshore current plus the zig–zag motion of the wave run-up transport beach material (sand in many situations) along shore as indicated. This is a dynamic longshore sand transport process under which a steady-state beach persists as long as the up-coast sand supply exists.

Of course, the wave run-up must return to the ocean. This return flow is concentrated in narrow rapidly moving offshore moving currents called rip currents (Fig. 2.22).

2.5 Wind-Forced Ocean Processes

2.5.1 Frictional Effects

Surface winds apply stress to the ocean surface to generate upper ocean currents and produce turbulent mixing. This process of transferring momentum to the ocean currents occurs through a complex process involving the generation of surface waves. In contrast, less complex stress-related processes remove momentum from near-bottom ocean flows and dissipate it as heat. Thus, ocean stress in the ocean mediates the vertical transport of horizontal momentum in the ocean.

The normal expression for fluid stress, in which horizontal stress τ is proportional to the local vertical gradient of horizontal velocity, is given by

$$\tau = \mu \frac{\partial u}{\partial z} , \tag{2.9}$$

in which μ is the coefficient of molecular viscosity. However, μ is too small for this relation to accurately define momentum transport (and thus stress and dissipation) in a turbulent ocean. Thus, we must incorporate turbulent eddy viscous effects into our consideration of momentum transfer in the ocean.

The nature of eddy viscous effects can be defined quantitatively by partitioning a variable eastward ocean flow into its temporal mean value $\overline{u}$ and eddy-induced fluctuating part u' (Fig. 2.23). A similar treatment defines the fluctuating *northward* and *upward* velocity components v' and w', respectively.

The time-average of the many random turbulent eddy events involving correlated fluctuations $\overline{u'w'}$ leads to an effective eastward stress S_x on a horizontal face of the fluid. The result is a turbulence-induced stress – called a Reynolds stress – that can be related to the shear of the mean flow via a coefficient of *eddy dynamic viscosity* A^e according to

$$S_x = A_z^e \frac{\partial \overline{u}}{\partial z} = -\rho \overline{u'w'} , \tag{2.10}$$

where $\nu_z^e = A_z^e/\rho$ is the *eddy kinematic viscosity*.

Similar relationships can be derived for stresses on other *faces* of a water parcel. Typical vertical eddy kinematic viscosities in the ocean range from 2 to $10^4\,\mathrm{cm^2\,s^{-1}}$. Lateral kinematic eddy viscosities are generally larger ranging from 10 to $10^8\,\mathrm{cm^2\,s^{-1}}$. The large difference between the vertical and lateral eddy coefficients relates to the fact that vertical turbulent momentum transport is considerably reduced relative to lateral momentum transport. This asymmetry is due to both the large geometrical aspect ratio or *thinness* of oceans; as well as the stabilizing effects of vertical stratification of the ocean.

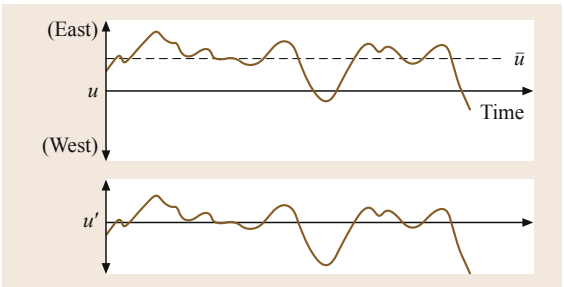

Fig. 2.23 The total time-varying of say an eastward flow is $u(t)$, which can be partitioned into its time-averaged component $\overline{u}$ and fluctuating component u'

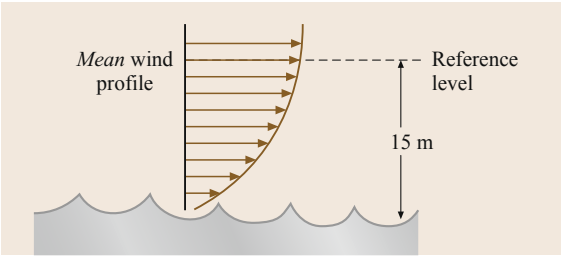

Fig. 2.24 Typical boundary layer air flow near a solid (or watery) horizontal boundary shows the effects of momentum extraction from the flow. The reference level of the wind at 15 m above the sea surface is used for estimating horizontal wind stress at the air-ocean interface

These considerations apply directly to oceanic stresses at the air–ocean and ocean–sediment interfaces. For example, dimensional considerations allows us to estimate sea surface stress according to is estimated as a function of the

$$\tau_w = \text{constant} \cdot \rho_a W_{15}^2 \,, \tag{2.11}$$

where W_{15} is the wind velocity at 15 m above the sea surface – the elevation of many ship and buoy anemometers.

To determine the constant in (2.11) we first define a friction velocity u^* such that $\tau = \rho_a u^{*2}$. Then consider the surface layer of turbulent winds near the sea surface – or *boundary layer* – with a time average wind profile that decreases from a maximum at the top of the boundary layer to near zero at the sea surface (Fig. 2.24).

It can be shown that the mean velocity profile $\overline{u(z)}$ in a constant stress turbulent boundary layer can be described in terms of a friction velocity u^* and Von Karman's constant $k_o = 0.4$ according to

$$\overline{u}(z) = \frac{u^*}{k_o} \ln \frac{z + z_o}{z_o} \,, \tag{2.12}$$

where z_o is a parameter related to ocean surface roughness. This form of the boundary layer mean velocity is the so-called Log Profile. This formulation permits us to compute u^* and z_o from the observations of $\overline{u}(z)$ so that the unknown constant in an expression for wind stress can be determined. Typically

$$\tau_w = 2.6 \times 10^{-3} \cdot \rho_a W_{15}^2 \tag{2.13}$$

for density units g cm^{-3} and wind units m s^{-1}.

The wind stress exerted on the sea surface can be expressed in terms of the direction of the wind vector $\boldsymbol{W}$ and is proportional to the square of the wind speed according to the relation

$$\boldsymbol{\tau}_w = \rho_a C_D |\boldsymbol{W}| \boldsymbol{W} \,, \tag{2.14}$$

where ρ_a is the air density and C_D is a drag coefficient.

2.5.2 Earth Rotation Effects

Earth rotation plays a central role in the physics (as viewed in our earthly rotating – hence accelerating frame of reference) of many of the most important atmospheric and ocean flows, (which have variability time scales exceeding 1/2 day). Earth rotation (rate $= \boldsymbol{\Omega}$) influences ocean flow through the effects of the Coriolis force which always acts to the right of the direction moving water (Fig. 2.25) according to

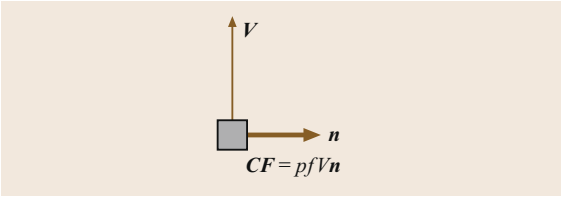

Fig. 2.25 An ocean water parcel is moving in an arbitrary direction with steady velocity $\boldsymbol{V}$ in the Northern Hemisphere. The Coriolis force $\boldsymbol{CF}$ acts on a moving water parcel to the right of the direction of $\boldsymbol{V}$ – or in the $\boldsymbol{n}$ direction

$$\boldsymbol{CF} = \rho f \boldsymbol{V} \boldsymbol{n} \,,$$

where ρ is the water density, $f = 2\Omega \sin(\text{latitude})$ is the Coriolis parameter, $\boldsymbol{n}$ is the unit vector in the direction perpendicular and to the right of the water parcel velocity $\boldsymbol{V}$ composed of an eastward u and northward v components.

In the Northern Hemisphere Cartesian coordinate system, the Coriolis force $\boldsymbol{CF}$ is given by $\boldsymbol{CF} = \rho f v \boldsymbol{i} - \rho f u \boldsymbol{j}$; where $i \neq j$ are the unit vectors in the eastward and northward directions, respectively.

2.5.3 Hurricane Wind-Forced Ocean Response

Tropical cyclones have a significant impact on coastal areas of the world. In the Atlantic Ocean they are called hurricanes, whereas similar storms in the Pacific Ocean are called typhoons. They are a significant part of global weather systems because they transfer large quantities of water and warm, moist air from equatorial regions to higher latitudes. In the Caribbean Sea, the Gulf of Mexico, and the southeastern United States, hurricanes have shaped low-lying coastal areas and, at times, have caused dramatic losses of life and property.

Historically, the hurricane season in the North Atlantic Ocean has extended from June 1 to November 30; when seawater temperatures in the equatorial oceans are warmest, usually above 25 °C (about 80 °F). Hurricanes begin as tropical waves, areas of organized clouds 200–500 km in diameter in the eastern equatorial Atlantic. Occasionally, the wave becomes a tropical depression, which when winds become 65–118 km/h (39–74 mph) becomes a tropical storm, which propagates generally westward. If winds exceed 118 km/h, the storm is called a hurricane (in the Atlantic and eastern Pacific oceans) or a typhoon (in the western Pacific Ocean) – powerful, self-sustaining atmospheric/oceanic heat engines.

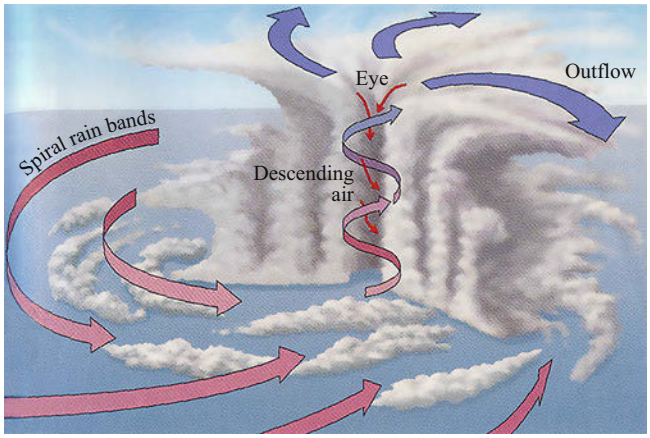

Fig. 2.26 Typical hurricane wind/cloud structure (after [2.11])

Tropical storms and hurricanes have cyclonic or counterclockwise circulation in the Northern Hemisphere because the Coriolis effect deflects the inward air flow toward to the right (Fig. 2.26). (In the Southern Hemisphere, the Coriolis deflection is to the left so that cyclones in the southern tropics have clockwise rotation). In a hurricane, inward flowing air spirals in an anticlockwise sense over the warm, wet ocean toward the eye, where it begins to spiral upward around the *eyewall* that surrounds the eye of the hurricane. As the air rises it cools and its water vapor condenses forming clouds and rain and releasing heat that propels the air even higher. At the top of the eyewall, most of this very cool, dry air begins to descend into the eye and the various spiral bands, warming and becoming even less humid (i. e., dryer) as it encounters the higher pressures at lower levels.Upon reaching the sea surface this very warm, dry air is able to absorb both heat and moisture from the ocean enabling it to rise again, thus re-energizing the hurricane which continues to propagate under its own power.

Table 2.4 The Saffir–Simpson hurricane scale is based on the minimum sustained wind speed criteria for each of the official categories. Typical minimum surface atmospheric pressures and storm surges are given along with more subjective damage descriptions (after [2.10])

Hurricane category	Maximum sustained wind speed		Storm surge [ft]	Minimum Surface pressure [mbar]	Damage
	kilometers/hour	miles/hour			
1	119–153	74–96	4–5	> 980	Minimal
2	154–178	97–111	6–8	979–965	Moderate
3	179–210	112–131	9–12	964–945	Extensive
4	211–250	132–155	13–18	944–920	Extreme
5	> 250	156+	18+	< 920	Catastrophic

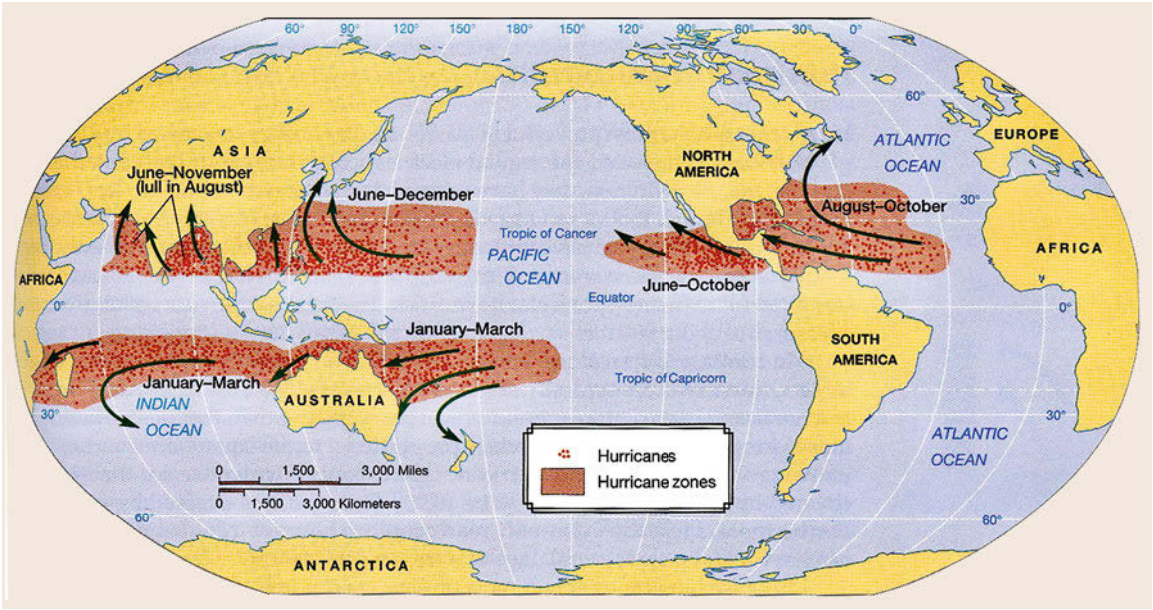

Fig. 2.27 Hurricane and typhoon locations around the globe (after [2.11])

The strength of hurricanes is measured by the Saffir–Simpson scale (Table 2.4), which uses minimum sustained wind speeds to categorize storms from Category 1, a minimal hurricane, to Category 5, the most intense hurricane. A list of the most intense US hurricanes appears in Table 2.5.

Hurricane trajectories are also influenced by larger scale meteorological forces – hence the uncertainty. Under certain conditions, the Atlantic hurricane trajectories tend toward the Caribbean, Florida and Gulf of Mexico; like hurricane Katrina in 2005 (Figs. 2.27 and 2.28). Under some conditions, the trajectories can take more northward paths along the eastern US seaboard; like hurricane Carol of 1954.

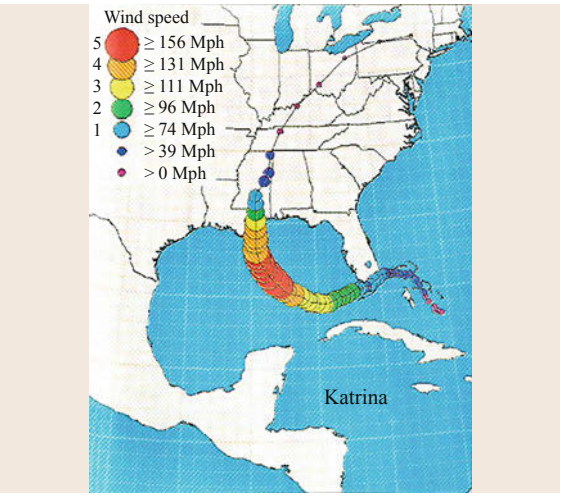

Fig. 2.28 The trajectory of hurricane Katrina showing the evolution in minimum sustained wind intensity and category (after [2.12])

The hurricane–ocean interaction also produces ocean surface waves, currents, and sea level changes or so-called storm surge. The group speeds of the most energetic (i. e., long) hurricane-generated surface waves are faster than typical hurricane propagation speeds and thus they speed out ahead of the hurricane. The local hurricane-generated ocean currents in the near-surface layer are intensified in the direction of the generating winds as the hurricane passes overhead. In the Northern Hemisphere, the highest hurricane winds are on the right hand side of the leading edge of the hurricane (the upper right quadrant in Fig. 2.29). This is because the forward speed of the hurricane itself adds to the speed of the wind around the storm on the right side of the storm.

As a hurricane approaches land, these ocean currents impinge on the land and thus can contribute to increased the sea level rise or storm surge. The storm surge is composed of contributions from the hurricane-generated current field and the elevated sea level that is induced by the very low sea level atmospheric pressure at the center of a hurricane. Thus the storm surge for a particular hurricane generally evolves in varying

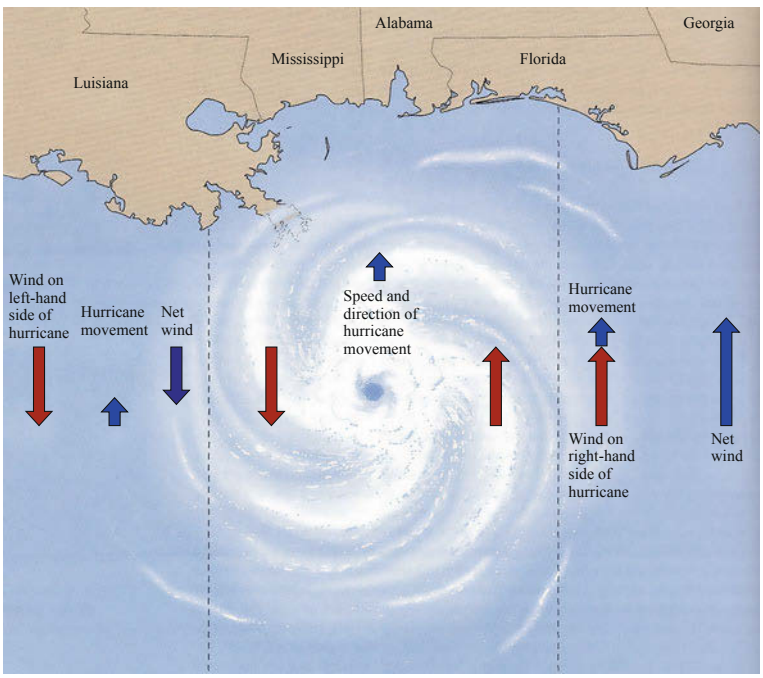

Fig. 2.29 Hurricane horizontal wind structure (after [2.7])

Table 2.5 Characteristics of the most intense hurricanes that made landfall in the US between 1900 and 1996 in terms of their categorization and central air pressure (after [2.10])

Hurricane	Year	Category	Pressure[a] [mb]	[in Hg]	[mm Hg]
Gilbert	1988	5	888	26.2	666.1
Florida Keys	1935	5	892	26.35	669.2
Camille	1969	5	909	26.84	681.7
Andrew	1992	4	922	27.23	691.6
Florida Keys/S. Texas	1919	4	927	27.37	695.2
Lake Okeechobee, Fl.	1928	4	929	27.43	696.7
Donna	1960	4	930	27.46	697.5
Galveston, TX	1900	4	931	27.49	698.2
Grand Isle, LA	1909	4	931	27.49	698.2
New Orleans, LA	1915	4	931	27.49	698.2
Carla	1961	4	931	27.49	698.2
Hugo	1989	4	934	27.58	700.5
Miami, FL/Pensacola, FL	1926	4	935	27.61	701.3
Hazel	1954	4[b]	938	27.70	703.6
SE FL/SE MS/AL	1947	4	940	27.76	705.1
North Texas	1932	4	941	27.79	705.9
Opal	1995	3[b]	942	27.82	706.6
Frederic	1979	3	946	27.94	709.7
Betsy	1965	3	948	27.99	710.9
Fran	1996	3	954	28.17	714.8

[a] Pressure exerted by the atmosphere at sea level is equal to 1 atmosphere, which is equal to 760 mm of mercury (760 mmHg), 1.01325 bar, 1013.25 mar, 29.92 inches of mercury (29.92 in Hg), and 14.7 pounds per square inch (14.7 psi)
[b] Hurricanses traveling more than 50 km/h.

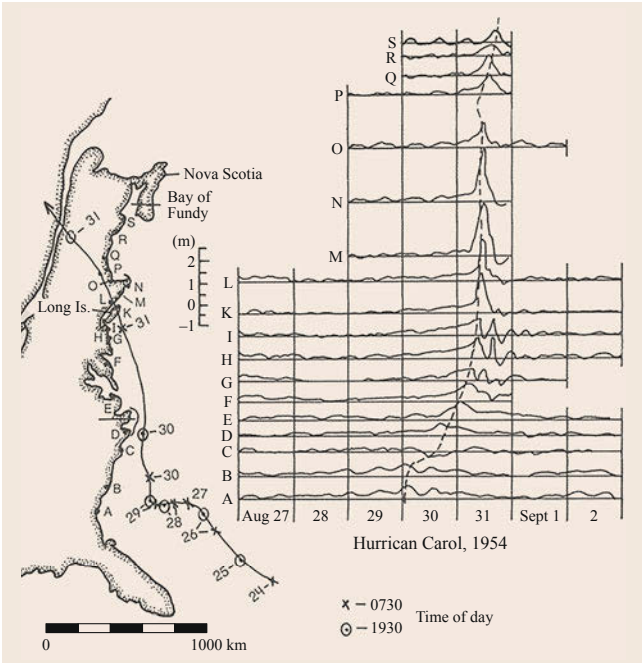

Fig. 2.30 The propagation of hurricane Carol along the US East Coast induced storm surge at coastal locations as hurricane Carol (after [2.13])

ways in tandem with the evolving hurricane (Hurricane Carol 1954, Fig. 2.30). Hurricane damage is caused by the combination of high winds, flooding, and storm surge. Surface winds can cause an abnormal (i. e., non-tidal) rise in sea level, reaching 1–6 m above normal sea level. Along the Gulf Coast, the estimated 330 km/h winds of Hurricane Camille in 1969 caused a maximum storm surge of 8 m, with 3-m-high wind-driven waves atop the surge. The end result was a l0-m-high wall of water approaching the Mississippi coastline. Failure to evacuate caused significant loss of life.

Hurricane-forced ocean currents are transient and intense in proportion to the wind intensity. The Integrated Ocean Observing System (IOOS) high frequency radar network along the US East Coast measured surface currents induced by 29 October 2012 *Superstorm* Sandy – the meteorological combination of a tropical hurricane and an extra-tropical storm that made landfall in New Jersey at about 2000 EDT 29 October 2012. The maps in Fig. 2.31 show that Sandy's winds overwhelmed the normal Mid-Atlantic 10–40 cm/s primarily wind-driven current patterns (e.g., 2000 EDT 27 October 2012) a full 24 h before landfall (2000 EDT 28 October 2012). The Sandy-induced intensifying southward currents that exceeded 1 kt (≈ 50 cm/s).

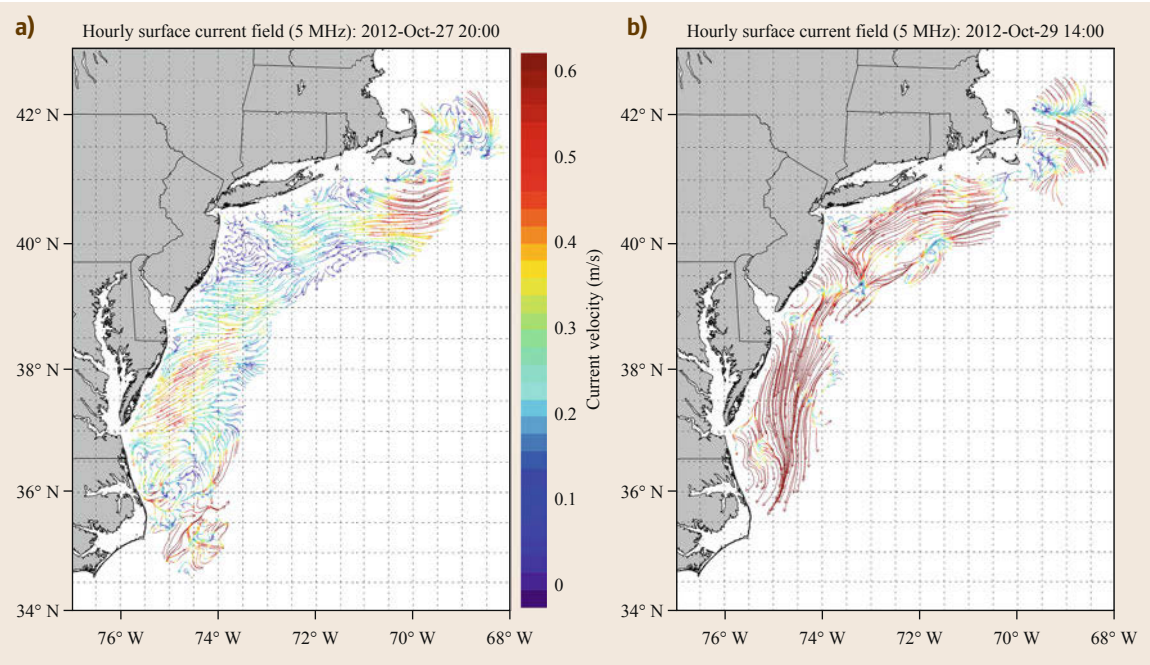

Fig. 2.31a,b Surface currents maps measured by a network of high frequency radar (HFR) sites in the coastal mid-Atlantic at: **(a)** 2000 EDT 27 October 2012 ... + 48 h before Superstorm Sandy landfall in New Jersey; and **(b)** 1400 EDT 29 October 2012 ... + 4 h – the last complete map before physical damage and power failures shut down the HFR network (after [2.14])

2.5.4 Wind-Forced Upper Ocean Response with Earth Rotation Effects

At time scale exceeding about one-half day, Earth rotation effects can become important. For example, in the aftermath of impulsive wind forcing, such as that associated with a weather front, the ocean often exhibits circular motion called inertial flow. More steady wind forcing of a frictional upper ocean often leads to Ekman flow. With larger scale wind shear, that forcing can induce Ekman divergence/convergence and associated upwelling and downwelling.

Inertial Flow

If there are no other significant horizontal forces present, then the Coriolis force will turn a moving water parcel into a clockwise (anticlockwise) circular inertial motion. The dynamics of *inertial motion* can be thought of as a dynamic balance between two pseudo-forces, namely the Coriolis force $\boldsymbol{CF}$ and the centrifugal force $\boldsymbol{f}_c$ that is associated with the acceleration of cir-

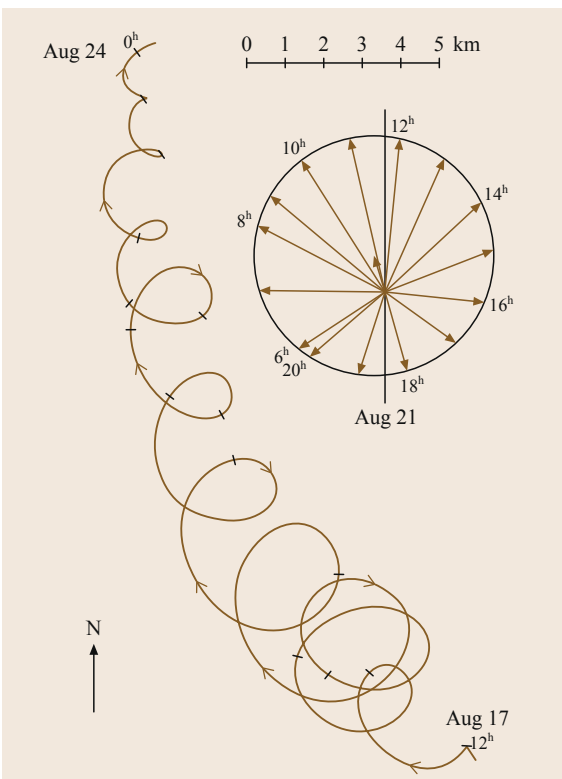

Fig. 2.32 A 7-day progressive vector diagram derived from moored current measurements time series, indicating clockwise circular inertial motion superposed on a northwestward flow (after [2.15]) ►

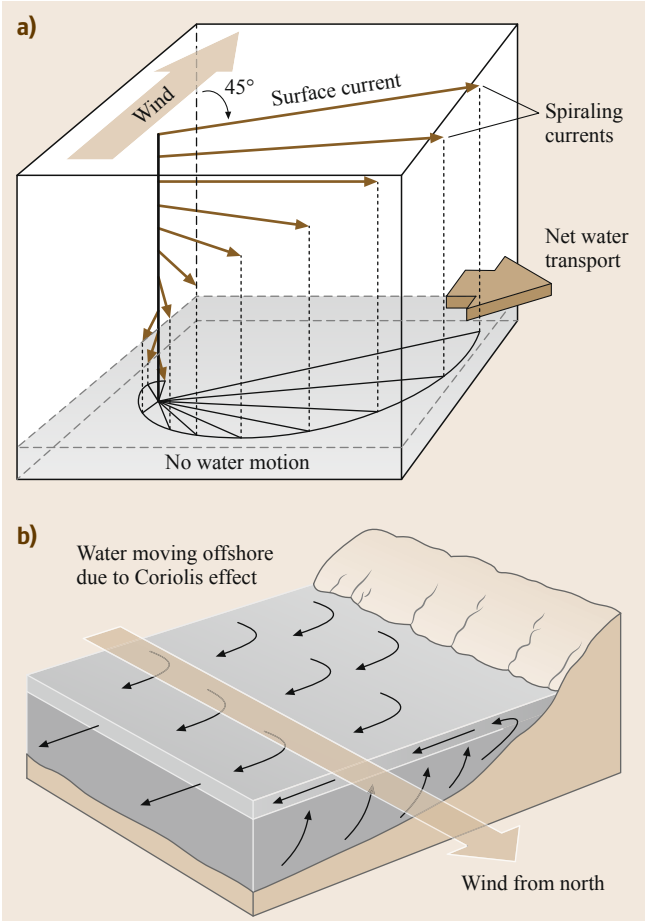

Fig. 2.33a,b Schematics of a Northern Hemisphere (NH) ocean being forced by a steady winds; showing **(a)** the surface velocity at 45° to the right of the surface wind stress and the downward spiral current structure – the vertical average of which yields a net Ekman transport to the right throughout the Ekman layer (after [2.7]). **(b)** Persistent winds along a NH coast produce a persistent Ekman transport *to the right* and an associated upwelling (after [2.10])

cular motion. Thus the force balance (per unit volume) for inertial motion is

$$\boldsymbol{CF} = \rho f \boldsymbol{V} = \rho \frac{\boldsymbol{V}^2}{R} = \boldsymbol{f}_c$$

so

$$f\boldsymbol{V} = \frac{\boldsymbol{V}^2}{R}$$

and the radius of the circle R

$$R = \frac{\boldsymbol{V}}{f} = \frac{\boldsymbol{V}}{2\Omega \sin\phi} .$$

The circular water parcel trajectory has an oscillation period called the inertial *period* T

$$T = \frac{2\pi R}{v} = \frac{2\pi}{f} = \frac{\pi}{\Omega \sin\phi}$$

which is independent of R! The inertial period is one half of a *pendulum day* which is defined as $2\pi/\Omega \sin\phi$. (A pendulum day is the time it takes for the vertical plane, in which pendulum swings, to rotate a full 360° (or 2π radians) relative to the Earth – a measure of the overhead Earth rotation rate at particular latitude). In practice, particularly after storm, it is not unusual to detect inertial motion (Fig. 2.32).

Ekman Flow

For wind stress-forced flow situations with times scales exceeding a half day, the effects of wind stress can be explored in terms a simplified form of the horizontal equations of motion in which Coriolis and frictional forces are balanced. The solution to these equations, assuming the application of a northward surface wind stress $\boldsymbol{\tau}_s = \tau_s \boldsymbol{j}$, is called *Ekman flow* whose respective eastward and northward components are

$$u^E = V_o e^{\pi z/D} \cos\left(\frac{\pi}{4} + \frac{\pi z}{D}\right) , \qquad (2.15a)$$

$$v^E = V_o e^{\pi z/D} \sin\left(\frac{\pi}{4} + \frac{\pi z}{D}\right) , \qquad (2.15b)$$

where $V_o = (\tau_s/\rho)/\sqrt{f\nu_z}$ is the surface velocity, $D = \pi\sqrt{2\nu_z/f}$ is the Ekman depth, and $\nu_z = A_z^e/\rho$ is the eddy kinematic viscosity.

While the detailed form of Ekman flow (Fig. 2.33) has only been recently verified experimentally, the existence of a vertically averaged flow to the right of the wind stress (Northern Hemisphere) called the Ekman transport has been observed for a long time. On ocean basin scales, as discussed below, Ekman transport convergence associated with the basin-scale wind fields create the conditions for large-scale ocean gyre currents. Near coasts, persistence along coast wind forcing generates offshore or onshore Ekman transports which lead to coastal upwelling/downwelling (Fig. 2.33). This process is particularly prominent along the US west coast during the summer when equatorward coastal winds persist.

2.5.5 Wind-Driven Currents: Ocean Basin Scale

Global-scale winds drive similar basin-scale gyre flows distinguished by intensified poleward flowing western boundary currents and less distinct equatorward flowing eastern boundary currents (Fig. 2.34). These mid-latitude gyre flows are connected by both tropical ocean current systems that straddle the equator in

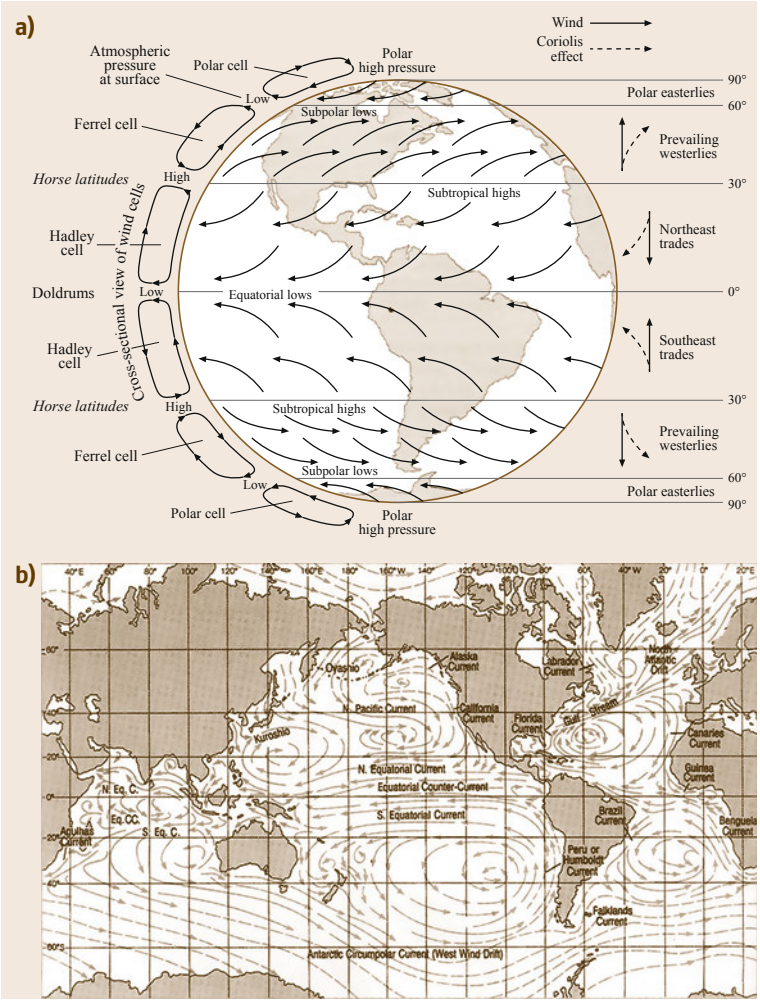

Fig. 2.34 **(a)** Average surface global winds divide into zonal bands due to Earth rotation effects. In both hemispheres, there are zones for the tropical easterly trade winds (equator–30°N and S), prevailing westerlies (30–60°N and S), and polar easterlies (60–90°N and S). **(b)** The major ocean basins feature gyre current systems that are interact through east–west equatorial current systems in the Atlantic and Pacific and the Antarctic Circumpolar Current in the Southern Ocean (after [2.7])

the Atlantic, Pacific, and Indian oceans and the Southern Ocean that circles Antarctica. The transports of the principal currents are presented in Table 2.6.

The dynamics of much of the open ocean flows is governed by one of the geostrophic force balances in which the Coriolis force balances the horizontal pressure gradient force for an arbitrary flow direction that is perpendicular to the force direction (Fig. 2.35).

The scalar form of the force balance is

$$\rho f|\boldsymbol{V}| = \frac{\partial p}{\partial n}$$

So that the geostrophic flow magnitude is

$$V_{\mathrm{g}} = |\boldsymbol{V}| = \frac{1}{\rho f}\frac{\partial p}{\partial n}\,.$$

Table 2.6 Transport of major ocean surface currents

Location	Name	Maximum current [cm/s]	Volume transport [10^6 m^3/s]
Western Boundary Currents	Gulf Stream	200–300	400
	Kuroshio Current	> 200	50
	Brazil Current	50–100	10
Southern Ocean	Antarctic Circumpolar Current	15	150
Equatorial Currents	North Pacific Equatorial Current	20	45
	Equatorial Undercurrent	100–150	40
Eastern Ocean	Peru Current	10–50	20

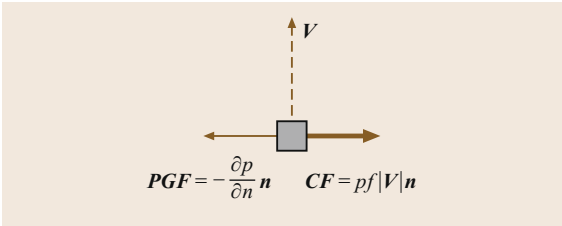

The Cartesian representation of the velocity, Coriolis force, and pressure gradient force are

$$\boldsymbol{V} = u\boldsymbol{i} + v\boldsymbol{j}\,,$$
$$\boldsymbol{CF} = \rho f v\boldsymbol{i} - \rho f u\boldsymbol{j}\,,$$
$$-\partial p/\partial n = -\partial p/\partial x\boldsymbol{i} + -\partial p/\partial y\boldsymbol{j}\,.$$

Strictly speaking geostrophic flow is a steady-state, rectilinear flow that is perpendicular to the Coriolis/pressure gradient force balance which is to the right (left) in the Northern (Southern) Hemisphere as illustrated in Fig. 2.35. However, geostrophic flow is a practical model because much of the open ocean flows vary slowly compared to a pendulum day with very little curvature. The pair of diagrams in Fig. 2.36 show how the ocean has adjusted its internal mass structure (through seaward flows of warmer water and landward flows of cooler water) to generate the appropriate sea surface slope-induced pressure gradients that balance the Coriolis forces associated with what is a primarily wind-driven Gulf Stream flow.

Fig. 2.35 Generalized geostrophic flow force balance between the Coriolis force $\boldsymbol{CF} = \rho f|\boldsymbol{V}|\boldsymbol{n}$ and negative pressure gradient force $\boldsymbol{PGF} = -(\partial p/\partial n)\boldsymbol{n}$, which are acting on a water parcel with a velocity $\boldsymbol{V}$ in the orthogonal direction. The Cartesian components of different vectors are given ◄

The combined prevailing westerlies and easterly trade winds in the subtropical latitude band between 10° and 50° set up a poleward sheared surface wind stress field (Fig. 2.34a) that drives the basin-scale geostrophic gyre flows in the principal ocean basins. The Ekman transport generated by the westerlies and the trade winds converges in the vicinity of 30° in both the northern and southern Atlantic and Pacific Ocean basins. This situation creates the tendency for east–west zonal geostrophic flow perpendicular to Ekman transport-induced north/south pressure gradients and Coriolis force. However, in most ocean basins (the exception being the Southern Ocean around Antarctica), continents block the zonal ocean flow. So this wind-driven oceanic pressure field is a steady-state high pressure cell around which the geostrophic flow circulates. The combined effects of the geostrophic flow around the pressure cells and the earth's rotation lead to clockwise (or counterclockwise) basin scale *wind-driven* gyres in the Northern (or Southern) Hemisphere ocean basins (Fig. 2.34b). The gyroscopic interaction between the gyre motion and earth rotation leads to intensification of gyre currents along the western bound-

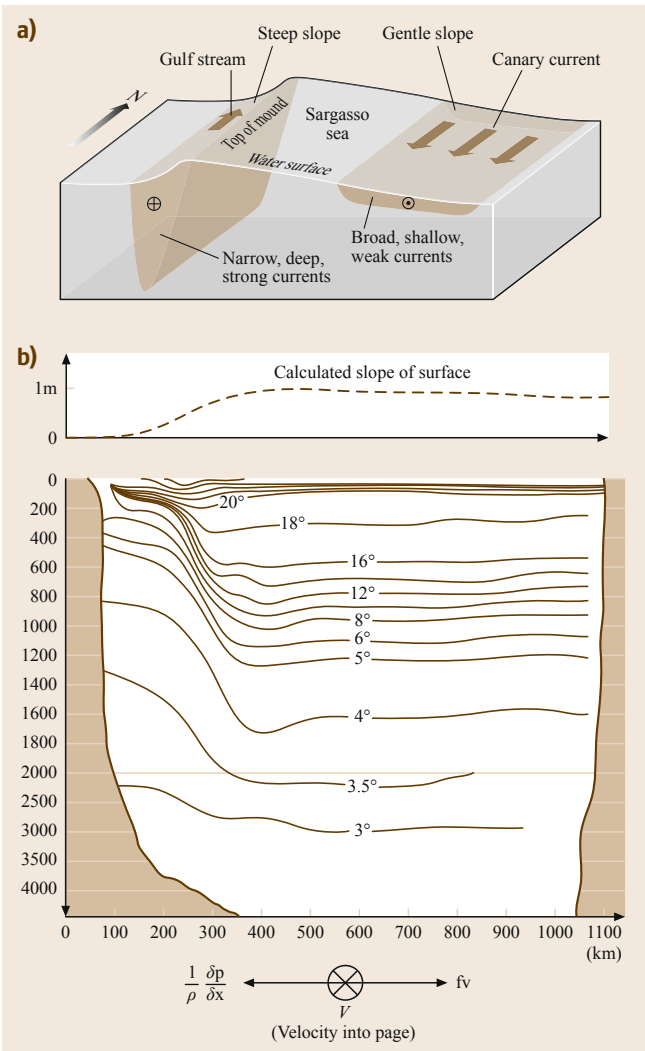

Fig. 2.36 **(a)** Schematic of the principal geostrophic flows in the North Atlantic basin. The exaggerated sea level distortions induce the pressure gradients that balance the Coriolis forces associated with the respective poleward Gulf Stream and equatorward Canary Current flows (after [2.7]). **(b)** A contoured temperature transect left-to-right across the Gulf Stream between Florida and Bermuda showing how the warm open ocean water raises sea level relative that associated with the cooler near-coast water and the relevant geostrophic flow force balance (after [2.6]) ◄

ary of all the ocean basins, exceeding 200 cm/s in the Gulf Stream of North Atlantic and in the Kuroshio of the North Pacific. The total transport of the Gulf Stream has been estimated to be in the range of 50–90 $\times 10^6$ m^3/s; with that of the Kuroshio being somewhat less (Table 2.6).

Despite the greater intensity of winds in the Southern Hemisphere, the intensity of the surface western boundary currents is less than that for either the Gulf Stream or Kuroshio. The Brazil current in the western South Atlantic has typical speeds of 50–100 cm/s and penetrates to depths of only about 400 m. in contrast to 800 m for the Gulf Stream. The reduced transport of the Brazil Current may be related to the presence of deeper western boundary undercurrents and their role in transporting heat poleward. The reduced intensity of the Australian current in the western Pacific and the Agulhas Current in the western Indian Ocean may be related to the lack of complete continental blockage of zonal flow.

The equatorward flow along the eastern boundaries of the wind-driven gyre as represented by the Canary and California Currents is generally less intense and less organized than the western boundary currents. The exception is the Benguela Current (Fig. 2.34b), which is an apparent extension of the Agulhas Current in the South Atlantic.

At tropical latitudes straddling the equator, significant trade winds can drive surface currents in the zonal circulation patterns shown in Figs. 2.34 and 2.37, patterns that exist in all major oceans. The wind-driven westward flow (Coriolis effects are weak near the equator) in a zone bracketing the equator is blocked by the presence of land masses. A resulting eastward pressure gradient force drives a return equatorial undercurrent jet along the equator and a seasonal countercurrent in the doldrum region. These countercurrents, while primarily zonal, are also very important connection between the major ocean basins.

The circulation at poleward latitudes greater than 50° differs greatly in the different oceans because of differences in the geography of the Northern and Southern Hemisphere ocean basins. The North Atlantic Ocean effectively ends at the sills at about 60°N and is weakly associated with the shallower Arctic Ocean, which has a circulation of its own. In the South Atlantic, there is a zonal ocean which circles the entire Antarctic continent. The winds are important in driving the broad Circumpolar Current (Fig. 2.34). Density adjustments in the interior produce pressure gradient forces which balance the Coriolis forces to produce a current profile which diminishes from about 15 cm/s at the surface to near zero at 3 km depth. So although Circumpolar Current speeds are considerably less than Gulf Stream speeds, the transports associated with the Circumpolar

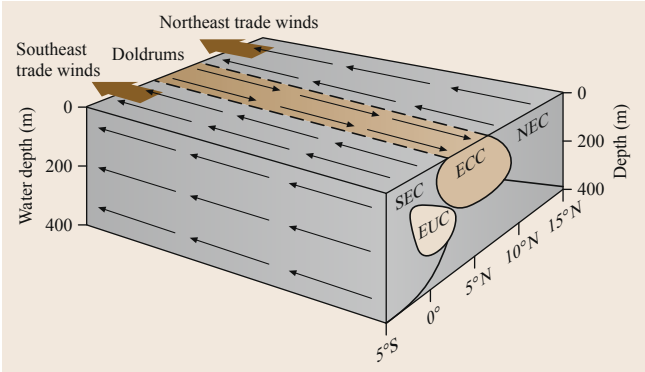

Fig. 2.37 Generalized Scheme of equatorial currents. Schematic of the westward trade wind-driven south (SEC) and north equatorial currents (NEC) bracketing the eastward flowing equatorial countercurrent (ECC) and equatorial undercurrent (EUC) (after [2.7])

Current are 130–190 $\times 10^6$ m^3/s and larger than Gulf Stream transports. As such, this current has the largest transport of any in the world's oceans and plays a crucial role in controlling the deep ocean circulation.

2.5.6 Gulf Stream Ring Flows

Before leaving the discussion of the wind-driven surface currents, it is important to note that western boundary currents are unstable leading to considerable changes on monthly time scales. For example, the Gulf Stream meanders and on occasion sheds pairs of eddies; warm core rings containing warm Sargasso Sea water or cold core rings (Fig. 2.38) containing colder waters with origins in the north. These rings are characterized by high currents – Gulf Stream-like currents of 50–100 cm/s. This eddy-shedding process enables effective poleward heat transport. Once these rings are shed, with the large Gulf Stream-like ocean currents, propagate affecting their local environments. Cold-core rings south of the Gulf Stream also propagate southwestward to be eventually entrained by the Gulf Stream in the region of Cape Hatteras. Warm-core rings with clockwise circulation are observed to propagate slowly southwestward along the continental margin on the northern side of the Gulf Stream. Satellite infrared imagery *is very* helpful in tracking these anomalously warm and cold eddies.

In reality, all of the upper oceans of the world are filled with eddy-like current structures embedded in the large-scale, wind-driven gyres described above. Typical currents in these eddies are about 10–20 cm/s. in contrast to the 1 cm/s gyre mean flow, and have lateral extents of about 100 km. Such eddies have been observed to propagate through a region in a period of months. The role of these eddies in the overall transport

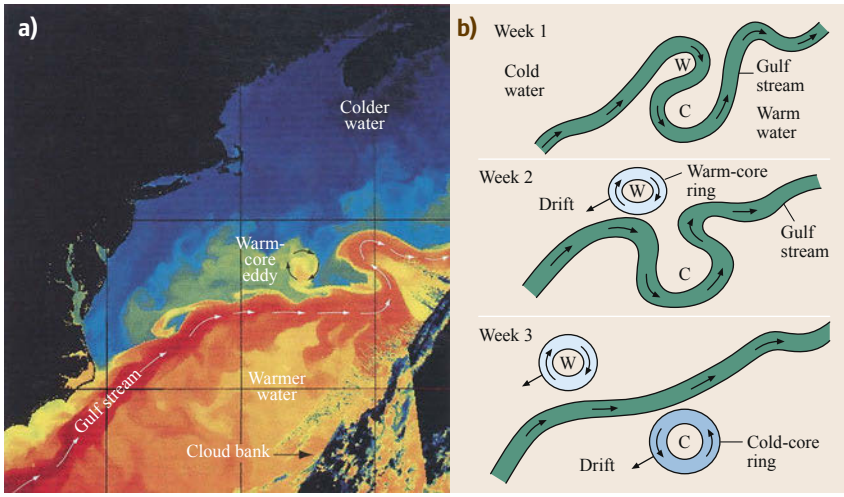

Fig. 2.38 **(a)** The warm Gulf Stream becomes unstable after leaving coast at Cape Hatteras, NC, and spawns both cold and warm core rings. **(b)** Gulf Stream ring formation begins with a meander that semienclosesses pockets of the warmer Sargasso sea water. and colder Slope Sea water. Every few months first a clockwise warm core ring and then an anticlockwise cold core ring will snap off. These rings will then drift equatorward on their respective side of the Gulf Stream – many times being reabsorbed by the Gulf Streams after several months of drifting (after [2.7])

of heat and other constituents is only just beginning to be understood.

The circulation in the tropical regions is likewise unsteady. A very important tropical ocean process is one in which warm equatorial waters in the western Pacific flow from west to east in response to moderating trade winds – with an uneven periodicity of 2 to 7 years. This anomalous flow of warm equatorial water has devastating effects on the fisheries along the Western Coast of South America. This ocean-centric process – called *El Nino* – is now known to be part of the larger scale atmospheric process called the Southern Oscillation. thus, the whole El Nino-Southern Oscillation process is referred to as ENSO.

2.6 Deep Ocean Currents

Superimposed on the wind-driven upper ocean circulation, which is mainly confined by the main pycnocline (or density gradient; Fig. 2.2) is a less intense thermohaline circulation. This global ocean scale overturning cell is driven primarily by atmospheric cooling-driven sinking of waters in the polar regions and closed through a poorly understood systems of vertical advections. The net effect of these vertical return flows (average vertical velocities of centimeters/day) is to maintain the depth of the main pycnocline against the downward heat diffusion in the upper ocean (Fig. 2.39).

Early ideas of deep ocean circulation were based on the ideas that water at polar latitudes – delivered primarily by western boundary currents – becomes relatively dense as it was cooled by the atmospheric winds and sank to depths in accordance with its density – with the coldest water sinking the deepest. As the water slowly warmed over hundreds if not thousands of years, it became less dense and rose to the surface distributed throughout the global oceans (Fig. 2.39).

The Stommel–Aron [2.16] dynamic theory of the thermohaline circulation of the world's oceans consisted of (a) polar region sinking – primarily North Atlantic and Antarctica – that (b) fed a network of deep western boundary currents (Fig. 2.40) that distributed the water to (c) a selected set upwelling zones from where (d) it returned to the upper ocean western boundary currents. Subsequent observations of the Atlantic deep western boundary current have verified one of the principal predictions of the Stommel–Aron theory.

Thus the overall picture of global ocean circulation is one that combines wind-driven and thermohaline flows in ways that transport enough heat poleward to

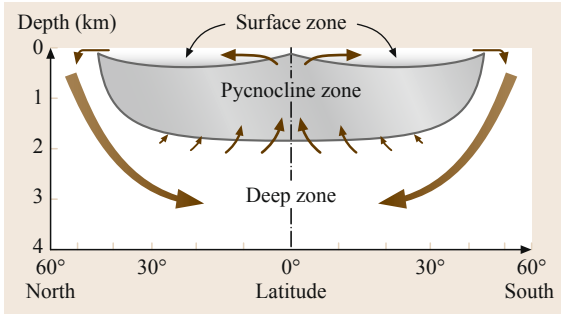

Fig. 2.39 Schematic of a three-zone global ocean in which thermohaline or meridional overturning circulation consists of poleward flow in the surface layers, sinking in the polar regions and upwelling through the very stable density gradient or pycnocline zone

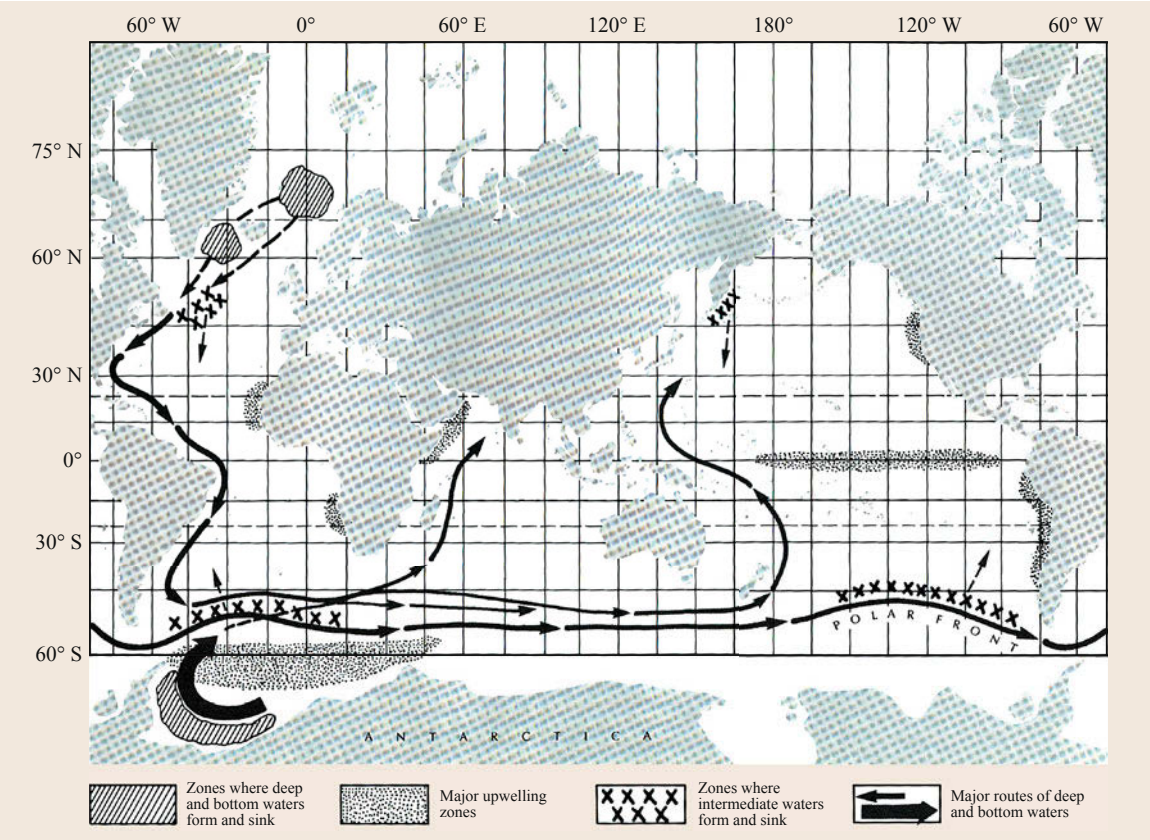

Fig. 2.40 The Stommel–Arons theory of deep ocean circulation consisting of a distributed set of deep western boundary currents that were connected via the Southern Ocean and to upwelling in the Southern, equatorial, and selected coastal oceans (after [2.4])

balance a polar hear deficit. The North Atlantic composite ocean circulation consists of an intense Gulf Stream that is opposed by the southward flowing deep western boundary currents composed of North Atlantic polar waters. The South Atlantic composite ocean circulation consists of a relatively weak Brazil current that is aided by a southward deep western boundary currents of North Atlantic polar waters. The medium intensity Kuroshio Current in the western Pacific is aided by deep underwater currents in transporting heat poleward.

2.7 Coastal Ocean Currents

The relative shallowness of the continental shelf and coastal regions of the world's oceans leads to a distinct current regime in which short term fluctuations are much larger than longer term mean flows. In general, the shallower coastal ocean waters respond more readily to wind forcing and exhibit important variability on the 2–10-day time scales of the mid-latitude synoptic weather systems which pass through the region. Density fronts caused in part by the proximity of the coastal ocean to significant fresh water river sources are associated with significant intensification of shelf and coastal currents. Of course, there are always tidal currents, which in many cases are as relatively weak (5 cm/s) as in the deep ocean. However, other places in the coastal ocean exhibit significantly stronger tidal currents that play a more important role in the mixing of shelf and coastal water masses (see next section for more on that).

Wind-forced shelf currents vary over longer time scales than tidal currents and thus are usually more effective in transporting nutrients, biota, pollutants, and other constituents on the shelf. Wind-forced

shelf fluctuations are usually most intense (typically 10–50 cm/s) in the along-shelf direction, with the maximum currents occurring at mid-shelf.

The presence of significant across-shelf density changes, such as those found along the East Coast of North America, leads to a modified current structure in which maximum along-shelf currents are concentrated in the density front along the outer shelf. These currents change over longer time scales in response to the more slowly changing density structures. Occasionally, deeper ocean currents in the form of Gulf Stream warm core rings penetrate onto the shelf and disturb the *normal* distribution of currents found there.

On many continental shelves, including the East Coast of North America, there is a more or less steady along-shelf flow superimposed on the fluctuating tidal, buoyancy-induced and wind-driven current field. Typical velocities of these steady flows are usually about 5–10 cm/s. Thus, while astronomical wind forcing plays an important role in shelf currents, their superimposition leads to complex and, as yet, unpredictable patterns crudely described by the characteristics discussed above.

2.8 Ocean Surface Tides

The astronomically forced surface gravitational tide has wavelengths that are long compared to the ocean depth and thus is a shallow water wave. Tidal waves are strongly forced by the motion of the earth relative to the moon and the sun and thus differ from *freely* propagating wind-generated surface gravity waves. Unlike most short period wind-driven waves, tidal waves have periods on the order of a day – enough to be influenced by the earth's rotation (Fig. 2.2).

The tidal response of the global oceans is complex because of the combined astronomical *tidal forcing* of the earth, moon and sun. The observed tides differ significantly from location to location because of the shallowness and geographical complexity of the global ocean basins. Observed tides throughout the world's ocean are composed of differing mixtures of both twice-a-day (semidiurnal) and once-a-day (diurnal) tidal variability. For example, the tides in Pakhoi, China (Fig. 2.41) are primarily once-a-day (or diurnal), while the tides in Port Adelaide, Australia are primarily twice-a-day or semidiurnal. Although the tides at both locations include both semidiurnal and diurnal tides, the minor tidal constituent is too small to detect except when the tidal range is small. Note that about every 14

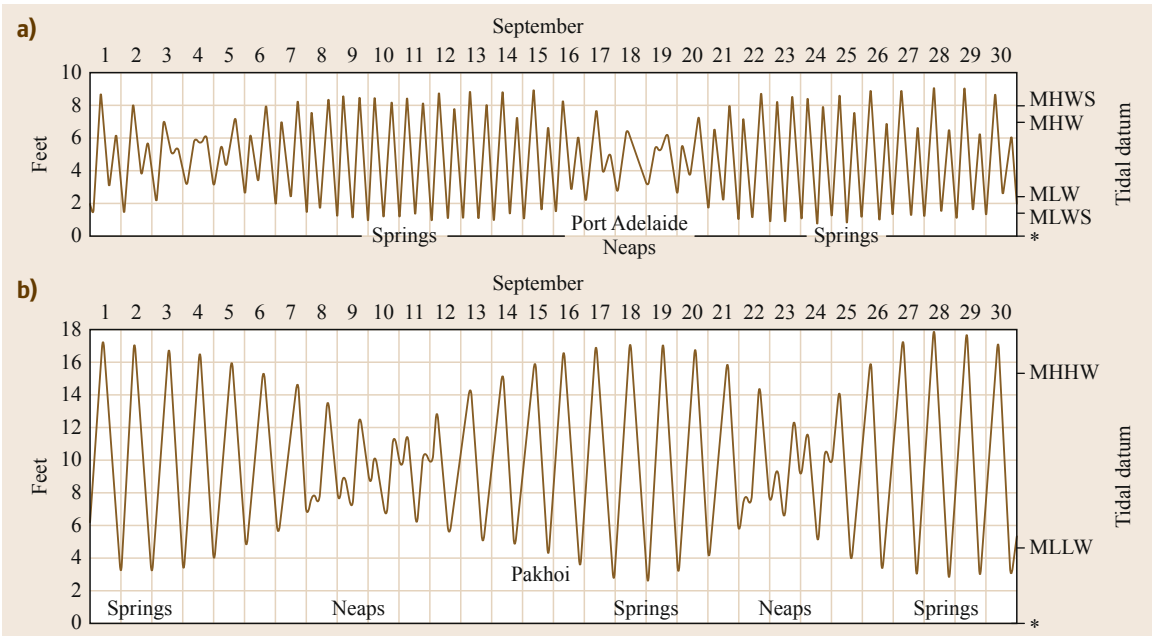

Fig. 2.41a,b Observed tides in **(a)** Port Adelaide are semidiurnal (twice-a-day) and in **(b)** Pakhoi diurnal (once-a-day). Tidal ranges in both locations exhibit a spring-neap cycles that are out of phase (after [2.15])

Table 2.7 The six basic astronomical tide-producing force frequencies are given in radians per unit time and degrees per solar day

Source	Angular frequency
Earth rotation	$\omega_\tau = \frac{2\pi}{\text{lunar day}} = 360° - 12.2°/d$
Lunar revolution	$\omega_s = \frac{2\pi}{\text{sidereal month}} = 13.176°/d$
Solar declination	$\omega_h = \frac{2\pi}{\text{solar year}} = 0.985/d$
Revolution of lunar perigee	$\omega_p = \frac{2\pi}{8.87\,\text{years}} = 0.111°/d$
Precession of lunar node	$\omega_N = \frac{2\pi}{18.6\,\text{years}} = 0.0529°/d$
Revolution of solar perigee	$\omega_{p1} = \frac{2\pi}{20\,000\,\text{years}} = 0.00005°/d$

days the range of the tidal sea level excursions and associated currents cycle through a maximum called spring tides and a minimum called neap tides (Fig. 2.41). This phenomenon occurs because the tide-producing forces associated with the moon and the sun reinforce (times of full and new moon) and oppose (times of half moons) each other twice a month.

As it turns out, there are five basic frequencies (Table 2.7) associated with astronomical tide- producing forces. Because the interaction of the astronomical tidal forcing and the oceanic response is highly nonlinear, the observed ocean tide anywhere on the earth can be decomposed into 400 *partial tides* (or *tidal species*). Each partial tides has a unique frequency ω_i that is determined by a set of integer weights a_j (for $j = 1, 2, 3, 4, 5,$ and 6) that multiply these six basic frequencies according to

$$\omega_i = a_1\omega_\tau + a_2\omega_s + a_3\omega_h + a_4\omega_p + a_5\omega_N + a_6\omega_{pl} \,.$$

Doodson [2.17] developed a shorthand notation for the weights called the Doodson number to define the different partial tides. (For example, the interaction of lunar declination changes and earth rotation leads to a pair of frequencies $\omega_\tau + 4\omega_s$ and $\omega_\tau - 4\omega_s$; which have Doodson number specifications (1 4 0 0 0 0) and (1 −4 0 0 0 0), respectively). The short list of the most important partial tides in Table 2.8 show equilibrium tidal forcing amplitude ratios relative to that of the M_2 tidal constituent – at many sites the most important constituent.

For practical purposes, the astronomical tide-producing forcing is fixed for all time. So the tidal response of the world's oceans, while it is complex spatially, is also fixed for all time. Thus to uniquely determine the tide at a particular location – say sea level $SL(t)$ – the task is to determine the amplitude (H_i) and

Table 2.8 List of the identities, periods, and relative equilibrium tidal amplitudes of the 19 of the most important partial tides (out of the 400)

Name of partial tides	Symbol	Speed (degrees per mean solar hour)	Period (solar hours)	Coefficient ratio $M_2 = 100$
Semidiurnal components				
Principal lunar	M_2	28.98410	12.42	100.0
Principal solar	S_2	30.00000	12.00	46.6
Larger lunar elliptic	N_2	28.43973	12.66	19.2
Luni-solar semidiurnal	K_2	30.08214	11.97	12.7
Larger solar elliptic	T_2	29.95893	12.01	2.7
Smaller lunar elliptic	L_2	29.52848	12.19	2.8
Lunar elliptic second order	$2N_2$	27.89535	12.91	2.5
Larger lunar evectional	η_2	28.51258	12.63	3.6
Smaller lunar evectional	λ_2	29.45563	12.22	0.7
Variational	μ_2	27.96821	12.87	3.1
Diurnal components				
Luni-solar diurnal	K_1	15.04107	23.93	58.4
Principal lunar diurnal	O_1	13.94304	25.82	41.5
Principal solar diurnal	P_1	14.95893	24.07	19.4
Larger lunar elliptic	Q_1	13.39866	26.87	7.9
Smaller lunar elliptic	M_1	14.49205	24.86	3.3
Small lunar elliptic	J_1	15.58544	23.10	3.3
Long-period components				
Lunar fortnightly	M_1	1.09803	327.86	17.2
Lunar monthly	M_m	0.54437	661.30	9.1
Solar semiannual	S_{sa}	0.08214	2191.43	8.0

phase (κ_i) for each of the partial tides (or *tidal constituents* η_i with its own ω_i) given by

$$\eta_i = H_i \cos(\omega_i t + \kappa_i) \; .$$

The harmonic constant H_i/κ_i pairs for each of the partial tides can be obtained by a harmonic analysis of a sufficiently long measured record – in this case sea level $SL(t)$ – from the site of interest. Modern harmonic analyses of measured records are based on a spectral analysis that has been modified to consider the variability at only the special partial tidal frequencies. Once determined, the partial tides can be constructed and summed to produce the total astronomically forced tidal sea level record according to

$$h(t) = \sum_i \eta_i = \sum_i H_i \cos(\omega_i t + \kappa_i) \; .$$

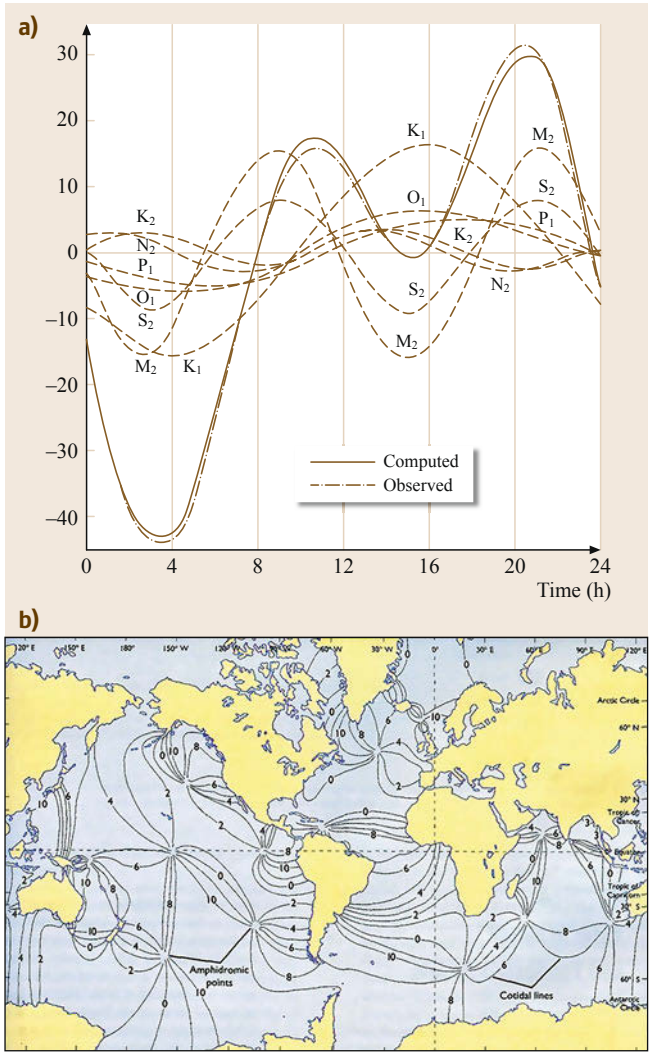

Fig. 2.42 (a) Harmonic decomposition of an observed sea level record (*dash-dot*) into several partial tidal constituents, which when added yield the computed tidal sea level (*solid*) part of the observed sea level record (after [2.10]). **(b)** The M_2 semidiurnal harmonic constants for an world's ocean array of sea level stations are used to construct a cotidal chart for the Atlantic Ocean tide. The solid cotidal lines mark the Greenwich times of high tide (after [2.7])

The harmonic constant H_i/κ_i pairs can be used to predict the future (present and past) tidal variability at the particular site. For most purposes, less than 10 tidal constituents are required to describe the tide adequately at a particular station. Figure 2.42a example shows the results of a tidal harmonic analysis of a sea level record in terms of seven tidal constituents. Note that this method is useful in predicting only that part of the measured sea level fluctuation which (2.1) occurs at astronomical frequencies and (2.2) is *phase locked* to the astronomical forcing.

Harmonic analysis results of a sea level record are widely useful because the principal contribution to sea level variability is usually at tidal frequencies. This helps to explain the relatively small difference between the observed sea level and the computed tidal sea level – a difference called the nontidal *residual sea level*. The residual or tidal signal *noise* can be of interest because it is due to other oceanic processes including weather forced phenomena, hydrodynamic nonlinearities, and wave phenomena at nontidal frequencies.

The maps of the harmonic constants can be used to define the patterns of the individual partial tides. The pattern of the very important M_2 semidiurnal tide is mapped for the Atlantic ocean in Fig. 2.42 – right in terms of its lines of constant tidal range (*cotidal lines*) and constant tidal phase (*copahse lines*). This *cotidal chart* for the M_2 semidiurnal tide reveals the classic signature of an *amphidromic system* in the North Atlantic; in which high tide, ranging from zero tidal range at its central *amphidromic point* to its maximum at its coastal extremes, marches around the basin in 12.42 h. The world's oceans consist of about six major interacting amphidromic systems.

The results of tidal harmonic analyses of ocean currents are more difficult to interpret than those from sea level because significant portions of ocean current variability (2.1) is due to wind – and not tidal forcing, and (2.2) even the tidal frequency variability is often are not phase locked to astronomical forcing. Internal gravity wave-generated currents can represent another major source of noise for the tidal harmonic analysis of currents. It is not unusual for internal wave currents with complex vertical structures to be superimposed on surface (or external) tidal currents with their more depth-

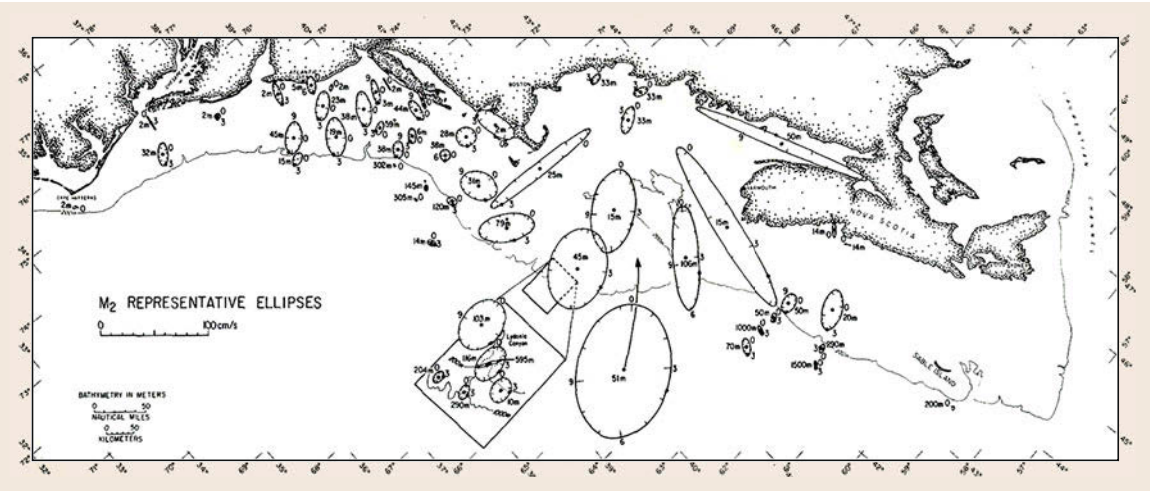

Fig. 2.43 Representative M_2 tidal current ellipses; representative of the mid-water column (water depths given). Ticks on ellipse edge indicated Greenwich hour, with the time of Boston high water indicated by the dot between hours 3 and 4. *Asterisks* identify currents 1 m above bottom, with bathymetry in meters (after [2.18])

independent structures. Therefore, relative to sea level records, current records need to be longer so that uncertainties in the tidal harmonic constants are comparable.

This guideline is less true for places like Georges Bank (at the entrance to the Gulf of Maine) where surface (or external) tidal currents forced by North Atlantic tidal variability dominate. This is because a large volume of water rushes into/out of the Gulf of Maine over the relatively shallow Bank during each semidiurnal tidal cycle. Because of earth rotation effects, semidiurnal tidal currents of more than 50 cm/s (≈ 1 nautical mile/hour or knot) rotate through a clockwise elliptical current vector pattern (for the M_2 semidiurnal ellipse see Fig. 2.43). Georges Bank tidal currents at are strongly sheared near the bottom, where their frictional effects transport sediments.

The amplitudes and ellipse characteristics of tidal currents vary greatly in the coastal ocean because of the effects of bathymetry and continental shelf configuration. The Gulf of Maine M_2 tidal current ellipses are larger than the rest of the northeast shelf region depicted in Fig. 2.43 because the Gulf of Maine length (Georges Bank – head of the Bay of Fundy) makes it is near-resonance with the semidiurnal tidal forcing.

2.9 Oceanic Internal Waves and Tides

With surface gravity waves, the air–sea density difference between air and water (ratio $\approx 1/800$) leads to the gravitational restoring force for fluid that has been displaced vertically (usually by wind). In the stably stratified water column, the similar, though weaker restoring force, makes *internal gravity waves* are possible. The surface expression of internal waves is very small, hence the name.

Consider the case depicted in Fig. 2.44a, where a thin layer (h') of less dense water ρ' overlies a thicker layer (h'') of slightly more dense water ρ''. Theory [2.19] indicates that an internal wave with wavelength L and phase speed of

$$c = \left[g h' \left(\frac{\rho'' - \rho'}{\rho''} \right) \right]^{1/2} ,$$

where $L/20 > h'$ and $L/2 < h''$ can arise. Thus the wave phase speed of a *shallow water* internal wave is considerably less than that of its surface gravity water counterpart because the reduced vertical density difference across the interface decreases the effect of gravity.

In contrast to the 2-layer example above, oceanic density and density gradients vary with depth or -z (Chap. 5). Internal gravity waves propagate in complicated ways throughout most of the ocean. Theory indicates that internal waves can occur at all depths in a stable water column between the frequencies of the inertial frequency $f(\phi) = 2\Omega \sin(\phi)$ (where ϕ is latitude) and the local buoyancy frequency that is given by

$$N(z) = \sqrt{-\frac{g}{\rho} \frac{\partial \rho_{pot}}{\partial z}} \quad \text{in radians/unit time} ,$$

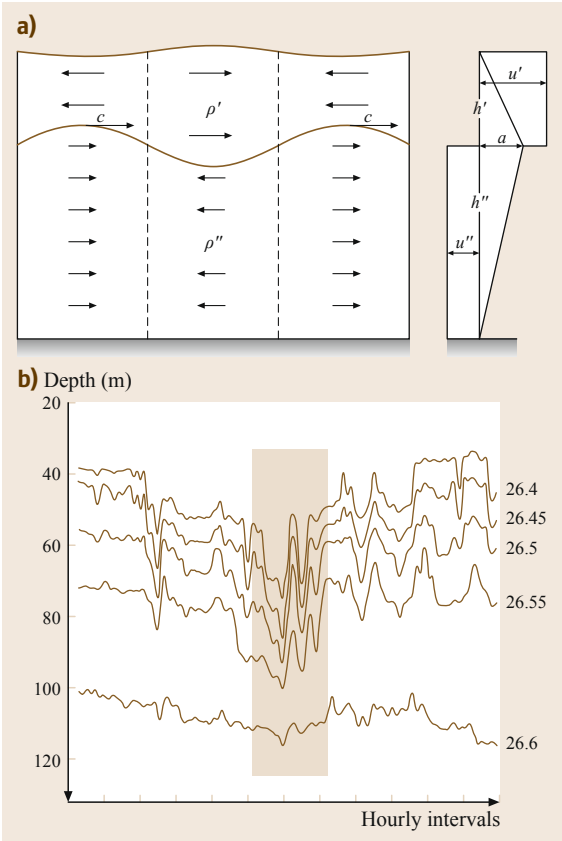

Fig. 2.44 **(a)** The configuration of an internal gravity wave in a 2-layer ocean with one layer of thickness h' and density ρ' overlying the deeper layer of thickness h'' and ρ'' supports an interfacial internal wave with a phase speed c that is independent of wave amplitude a (see text). Note the minor surface expression and that the opposed currents (u' and u'') in the respective layers do depend on the wave amplitude (after [2.8]). **(b)** Observed isopycnal depth time series define two rank-ordered oscillations on the trailing edge of an internal solitary wave of depression – estimated from moored observations on the northern California shelf in 133 m of water in April 21, 1981 (after [2.20])

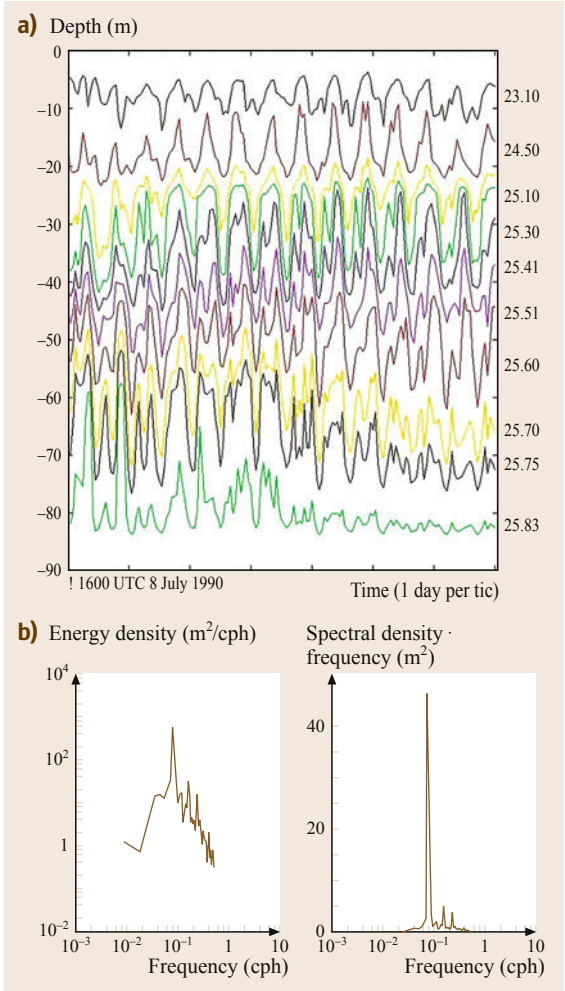

Fig. 2.45 **(a)** Massachusetts Bay isopycnal depth time series – inferred from density measurements – indicate strong internal tidal signatures throughout the water column. **(b)** Isopycnal displacement energy density spectrum. The prominent peak in the semidiurnal (≈ 12 h) frequency band is consistent with the proximity of the measurements to the internal tidal generation zone on Stellwagen Bank with 95% confidence limits indicated (b) Variance-preserving spectrum of the isopycnal displacement energy indicates the dominance of the semidiurnal internal tidal energy in the 12 h frequency band

where $-\partial\rho_{pot}/\partial z$ is the stable local gradient of potential density – a density that has been corrected for pressure effects (Chap. 5).

Intermittent interval wave events were observed by *Howell* and *Brown* [2.20] at a site in 133 m of water on the northern California continental shelf in April 1981. The water column at the site approximated a 2-layer ocean with an upper layer of 60 m. One of the observed events was a internal wave of depression with 29 m downward displacement of the mid-depth isopycnals (Fig. 2.44b), upper layer onshore velocity of 0.14 ± 0.02 m/s, lower layer offshore velocity of 0.14 ± 0.02 m/s, and time scale of 28 ± 4 min; all of which agreed well with internal soliton theory applied to the conditions of the observation site. They concluded that internal solitary waves, generated in the region of the continental slope, evolved into packets of solitons as they propagate shoreward before dissipating their energy of about 8.23×10^5 J per meter of wave crest.

The distribution of internal wave energy is determined by the nature of the different forcing mechanisms including winds and interactions between the surface tidal currents and bathymetry.

Temperature measurements made in the deep ocean (e.g., off Southern California and in the South China Sea) show significant concentrations of energy at semidiurnal frequencies. These temperature fluctuations were due to internal waves of tidal frequency (i. e., internal tides) with vertical displacement amplitudes of nearly 100 m and wavelengths of about 100 km. Evidence indicates that these energetic internal tides were generated at nearby bathymetric slopes.

Widespread evidence indicates that these internal tides represent an important component in the internal wave field many places in the world's oceans. In particular, subsequent interactions between (a) propagating internal tides from multiple generation sites, (b) the normally variable and heterogeneous oceanic density field, and (c) complex bottom bathymetry can lead to evolution and scattering that contribute to a general oceanic internal waves field with a range in periods that range between the local buoyancy (N) and inertial (f) frequencies. Other contributors to the oceanic internal wave field, include natural and well as ocean vehicle interactions with upper ocean stratification, with amplitudes that depend on the specific energetics of their generation processes.

The internal tide is an importantly energetic component of the internal wave field – particularly in the coastal ocean. One important and well-studied example of the internal wave being generated by surface (or external) tidal currents impinging on the bathymetric slopes is found on Stellwagen Bank in Massachusetts Bay. An array of moored measurements near Stellwagen Bank have been used to compute density time series at six levels; from which were produced the suite of isopycnal displacement time series shown in Fig. 2.45.

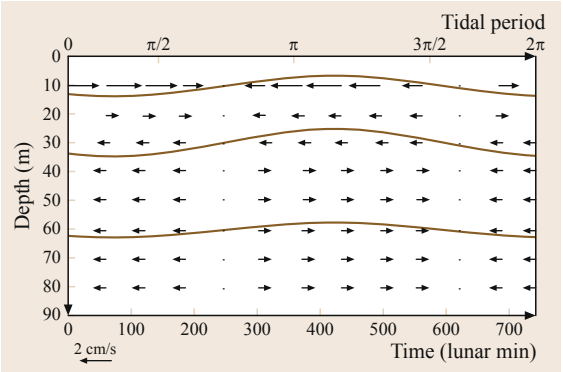

Fig. 2.46 Internal tidal kinematics: The spatial distribution of isopycnal displacement (−) and horizontal velocities associated with one cycle of an M_2 internal tidal wave in an ocean with exponentially decreasing buoyancy frequency

The energy spectra of these isopycnal time series clearly indicate the importance of the internal tide in the region (Fig. 2.45b). An analysis of these data has enabled us to construct the kinematical picture of the isopycnal displacement and current structure in Fig. 2.46. Note the zones of horizontal current convergence in the upper water column (strongest at the surface) and divergence at depth leading the isopycnal wave crest as it propagates from right to left. The current shear associated with such wave motion can become unstable leading to internal wave breaking and mixing.

References

2.1 R.A. Anthes: *Meteorology*, 6th edn. (Macmillian Publ., New York 1992)

2.2 G.L. Pickard, W.J. Emery: *Descriptive Physical Oceanography* (Pergamon, Oxford 1982)

2.3 A.C. Duxbury, A.B. Duxbury: *Introduction to the World's Oceans* (Addison-Wesley, Boston 1984)

2.4 S. Neshyba: *Oceanography Perspectives on a Fluid Earth* (Wiley, New York 1987)

2.5 B. Kinsman: *Wind Waves, Their Generation and Propagation on the Ocean Surface* (Prentice Hall, Englewood Cliffs 1965)

2.6 W.S. von Arx: *An Introduction to Physical Oceanography* (Addison-Wesley, Reading 1974)

2.7 P.R. Pinet: *Invitation to Oceanography*, 2nd edn. (Jones and Bartlett Publ., Sudbury 2000)

2.8 J.A. Knauss: *Introduction to Physical Oceanography* (Prentice Hall, Englewood Cliffs 1978)

2.9 V. Cornish: *Ocean Waves and Kindred Phenomena* (Cambridge Univ. Press, Cambridge, 1934)

2.10 B.W. Pipkin, D.S. Gorsline, R.E. Casey, D.A. Dunn, S.A. Schellenberg: *Laboratory Exercises in Oceanography*, 3rd edn. (Freeman, Macmillan Learning 2000), Online at http://www.macmillianhighered.com

2.11 E. Aguado, J.E. Burt: *Understanding Weather and Climate* (Prentice Hall, Upper Saddle River, 1999)

2.12 BAM, Courtesy of R. Sterner and S. Babin, Johns Hopkins University Applied Physics Laboratory

2.13 E. Bryant: *Natural Hazards*, 2nd edn. (Cambridge Univ. Press, Cambridge 2005)

2.14 MARACOOS: http://maracoos.org/blogs/main/?p=108

2.15 G. Neumann, W.J. Pierson Jr.: *Principles of Physical Oceanography* (Prentice Hall, Englewood Cliffs 1966)

2.16 H. Stommel, A.B. Arons: An idealized model of the circulation pattern and amplitude in oceanic basins, Deep Sea Res. **6**, 217–233 (1960)
2.17 A.T. Doodson: The harmonic development of the tide-generating potential, Proc. Roy. Soc. A **100**, 305–329 (1921)
2.18 J.A. Moody, B. Butman, R.C. Beardsley, W.S. Brown, P. Daifuku, J.D. Irish, D.A. Mayer, H.O. Mofjeld, B. Petrie, S. Ramp, P. Smith, W.R. Wright: Atlas of tidal elevation and current observations on the Northeast American Continental Shelf and Slope, US Geol. Surv. Bull. **1611**, 122 (1984)
2.19 H. Lamb: *Hydrodynamics*, 6th edn. (Cambridge Univ. Press, Cambridge 1932)
2.20 T.L. Howell, W.S. Brown: Nonlinear internal waves on the California continental shelf, J. Geophys. Res. **90**(c4), 7256–7264 (1985)